저작자표시-비영리-변경금지 2.0 대한민국

이용자는 아래의 조건을 따르는 경우에 한하여 자유롭게

- 이 저작물을 복제, 배포, 전송, 전시, 공연 및 방송할 수 있습니다.

다음과 같은 조건을 따라야 합니다:

저작자표시. 귀하는 원저작자를 표시하여야 합니다.

비영리. 귀하는 이 저작물을 영리 목적으로 이용할 수 없습니다.

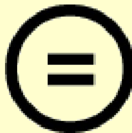

변경금지. 귀하는 이 저작물을 개작, 변형 또는 가공할 수 없습니다.

- 귀하는, 이 저작물의 재이용이나 배포의 경우, 이 저작물에 적용된 이용허락조건을 명확하게 나타내어야 합니다.
- 저작권자로부터 별도의 허가를 받으면 이러한 조건들은 적용되지 않습니다.

저작권법에 따른 이용자의 권리는 위의 내용에 의하여 영향을 받지 않습니다.

이것은 이용허락규약(Legal Code)을 이해하기 쉽게 요약한 것입니다.

Disclaimer

dCollection

이학박사 학위논문

Mapping the Nanoscale Effects of Charge Trap Activities on Local Carrier Transports in Inhomogeneous Two-dimensional Films

불균일한 이차원 필름에서 전하 트랩의 활동이 나노 스케일의 국소적인 캐리어 수송에 미치는 영향의 매핑에 관한 연구

2019년 2월

서울대학교 대학원

물리천문학부

양 명 재

Mapping the Nanoscale Effects of Charge Trap Activities on Local Carrier Transports in Inhomogeneous Two-dimensional Films

by

Myungjae Yang

Supervised by

Professor Seunghun Hong

A Dissertation Submitted to the Faculty of
Seoul National University
in Partial Fulfillment of the Requirements for the
Degree of Doctor of Philosophy

February 2019

Department of Physics and Astronomy

Graduate School

Seoul National University

Abstract

Mapping the Nanoscale Effects of Charge Trap Activities on Local Carrier Transports in Inhomogeneous Two-dimensional Films

Myungjae Yang
Department of Physics and Astronomy
The Graduate School
Seoul National University

In crystalline materials, there exist various defects such as vacancies, dislocations and grain boundaries, which generate additional electronic states called charge traps. Charge traps are localized states within the band gap of an electronic band structure. These states restrict the flow of charge carriers by randomly trapping carriers and releasing the carriers after a period of time. Furthermore, traps can also play a significant role in carrier transports, and thus, investigating trap activities are important to understanding electrical properties of materials. The trap activity, the trap-and-release of charge carriers, induces a fluctuation in the number of carriers in a conduction channel. As a result, an electrical signal from

an electronic device includes noise which randomly fluctuates over time. By measuring and analyzing electrical noise generated from an electronic material, we can obtain valuable information about internal structures and unique conduction properties of the material.

In this dissertation, it will be discussed about the effects of charge trap activities on local carrier transports in inhomogeneous two-dimensional films investigated via a scanning noise microscopy based on a conducting atomic force microscopy (AFM).

First, we will discuss nanoscale “noise-source switching” phenomena during the optoelectronic switching of phase-separated organic nanocomposites of tetrathiafulvalene (TTF) and phenyl-C_{61}-butyric acid methyl ester (PCBM) molecules dispersed in a polystyrene (PS) matrix. Here, a noise microscopy method was used to map the conductivity and charge trap density of the nanocomposite film with nanoscale resolution. Interestingly, when the nanocomposite was ‘set’ by a high bias, insulating PS-rich phases showed a drastic decrease in the density of charge traps which acted as noise sources. This could be attributed to the saturation of traps by charge carriers generated from a TTF-PCBM complex. Further, it was observed that conductivity had power-law relationships with local trap density, which implies the effect of charge traps on electrical conduction. The result provided evidence

for reversible modulation in charge trap activities during the switching cycle of an organic memory device.

Second, the anomalous enhancement of photoconductivity by localized charge traps in the grain structures of a molybdenum disulfide (MoS_2) monolayer will be discussed. Using a noise microscopy, we calculated the maps of sheet resistance and charge trap density for MoS_2 grain structures with nanoscale resolution. Importantly, we found an unusual inverse proportionality between the sheet resistance and charge trap density inside grains, which originated from the unique role of sulfur vacancies acting as both charge hopping sites and traps in monolayer MoS_2. In addition, under light illumination, regions with larger charge trap densities under dark conditions exhibited larger photocurrents, indicating that photocurrents were enhanced by local charge traps. We could explain the phenomenon by the act of oxygen molecules which were chemisorbed on sulfur vacancies under dark conditions and released electrons when they were desorbed by illumination.

Keywords: charge trap, defect, carrier transport, electrical noise, atomic force microscopy, scanning noise microscopy, two-dimensional film

Student Number: 2012-20370

Table of contents

Chapter 1 Introduction 1

1.1 Charge Trap 2

1.2 Electrical Noise 3

1.3 Scanning Noise Microscopy 6

1.4 References 8

Chapter 2 Noise-source Switching in Phase-separated Organic Nanocomposites 10

2.1 Introduction 11

2.2 Experimental Setup 13

2.3 Electrical Switching of Organic Nanocomposites 15

2.4 Noise-source Switching of an Organic Nanocomposite Film during an Electrical Switching Cycle 18

2.5 Effect of Charge Trap Activities on Local Carrier Transport in an Organic Nanocomposite Film 30

2.6 Optical Switching of Organic Nanocomposite by UV Exposure 40

2.7 Summary 46

2.8 References 48

Chapter 3 Enhancement of Photocurrent by Local Charge Traps in the Grain Structures of Monolayer Molybdenum Disulfide........... 52

3.1 Introduction 53

3.2 Experimental Setup.. 55

3.3 Characterization of a Monolayer MoS_2 Film.. 57

3.4 Mapping of Charge Trap Distribution in the Grain Structure of Monolayer MoS_2... 62

3.5 Effect of Charge Traps on the Hopping Transport of Charge Carriers in Monolayer MoS_2... 69

3.6 Photocurrent Enhancement by Local Charge Traps Generated from Sulfur Vacancies of Monolayer MoS_2 72

3.7 Summary.. 78

3.8 References 80

Chapter 4 Conclusions 84

Chapter 5 Abstract in Korean 86

List of figures

Figure 1-1 Noise spectrum showing fundamental noise. 3

Figure 1-2 Schematic diagram depicting the experimental setup of a scanning noise microscopy method on graphene. 6

Figure 2-1 Schematic diagram showing our noise microscopy setup for the polymer nanocomposite film on an ITO substrate. The current and noise signals were measured through a biased conducting probe by a homemade spectrum analyzer. 14

Figure 2-2 (a) Chemical structures of TTF (donor), PCBM (acceptor) and polystyrene (matrix). (b) Charge transfer mechanism in a donor-acceptor complex. 16

Figure 2-3 Mapping conductivity and charge trap density in the electrical switching cycle of a nanocomposite film. (a) AFM topography image of the nanocomposite film. (b) Current-voltage (I-V) curves measured on the sample. (c) Current map measured at the low bias of 0.1 V. (d) Current map measured in an area encircled with a yellow dashed line in (a) at the high bias of 1 V. (e) Current map obtained at the bias voltage of 0.1 V after the measurement of (d), on the region scanned for (c). (f) Current-normalized noise PSD (S/I^2) map (at 548 Hz) of the nanocomposite. (g) Conductivity (σ) map calculated from the current map in (e). (h) Charge trap density (N_T)

map showing the distribution of charge traps on the nanocomposite film. (i) Current map measured at the bias voltage of 0.1 V after we scanned a small region in the 'on state' area with the bias voltage of −1 V. (j) Topography image on the 'reset' region encircled with a green dashed line in (i). Scale bars are 1 μm. 19

Figure 2-4 Figure 2-4 Current map and lateral force microscopy image of a polymer nanocomposite film. (a) Current (*I*) map measured at the bias voltage of 0.1 V. (b) Lateral force microscopy image measured simultaneously with the current map. The image shows a separation between regions of *large* and *small* lateral force, which coincide with *low* and *high* current regions of the current map, respectively. 22

Figure 2-5 Relations between the conductivity (σ) and charge trap density (N_T) of the nanocomposite sample and schematics depicting charge transport and trap activities at each stage of a switching cycle. (a) Scatter plot σ and N_T in an 'off state'. Data from *TTF-PCBM-rich* and *PS-rich* phases are shown with *red* and *black* colors, respectively. (b) Energy level diagram of an 'off state' at the bias of 0.1 V. (c) σ *versus* N_T plot when the sample was 'set' by a high bias. (d) Energy level diagram during a set process with the high bias of 1 V. (e) σ *versus* N_T plot after the nanocomposite was 'set' to an 'on state'. (f) Energy level diagram of an 'on state' at the bias of 0.1 V. (g) σ *versus* N_T plot when the sample was 'reset' by a high reverse bias. (h) Energy level diagram during a reset process with the negative bias of −1 V. 31

Figure 2-6 Frequency dependence of current-normalized noise PSD (S/I^2) in an 'off state' (black) and during a set process (red). The S/I^2 of an 'off state' exhibited a $1/f$ noise behavior. On the other hand, a $1/f^{3/2}$ behavior was observed in the set process. 36

Figure 2-7 Effect of an optical switching by UV exposure on the nanocomposite film. (a) Schematic diagram showing a setup for UV exposure on the nanocomposite sample. (b) Topography image of the film after the UV exposure. The exposed area is encircled with a yellow dashed line. (c) Current (I) map after the exposure, measured at the bias of 0.1 V. (d,e) High resolution topography image of the (d) unexposed and (e) exposed areas. (f,g) Conductivity (σ) map of the (f) unexposed and (g) exposed areas. (h,i) Charge trap density (N_T) map of the (h) unexposed and (i) exposed areas. (j,k) σ *versus* N_T plots for the (j) unexposed and (k) exposed areas. Scale bars are 5 μm. 41

Figure 3-1 Schematic diagram depicting the scanning noise measurement setup for a MoS_2 monolayer sample grown onto a SiO_2/Si substrate. A conducting AFM probe laterally scanned the MoS_2 surface under ambient conditions, while making direct contact with the sample. Electrical current and noise PSD maps were simultaneously measured through the probe. The measured data were analyzed to obtain maps of the sheet resistance and charge trap density distributions in MoS_2 grain structures. 56

Figure 3-2 Characterization of a monolayer MoS_2 sample. (a) Optical

image of monolayer MoS_2 grown onto a SiO_2/Si substrate. (b) Raman spectroscopy data for the sample. (c) Current-voltage (I-V) curve measured on the sample. (d) Current measured by sweeping a gate voltage (V_G). The threshold voltage (V_{Th}) was estimated to be ~−40 V. (e) Current-normalized noise PSD (S_I/I^2) dependence on frequency. (f) S_I/I^2 at 30 Hz as a function of V_G. The slope of the fitted line is −1.994. 58

Figure 3-3 Thickness profile of CVD-grown monolayer MoS_2. (a) AFM Topography image of a monolayer MoS_2 sample. Dark regions are SiO_2. (b) Height profile along a red dotted line in (a). The thickness was ~0.7 nm. 59

Figure 3-4 Mapping of sheet resistance and charge trap density in the grain structure of a MoS_2 monolayer. (a) AFM topography image of the MoS_2 monolayer film. (b) Current (I) map of the MoS_2 film. A bias voltage of 5 V was applied to the film through a metal electrode. (c) Current-normalized noise PSD (S_I/I^2) map (at 17.3 Hz) for the film. (d) Sheet resistance (R_s) map for the MoS_2 sample. (e) Charge trap density (N_{eff}) map for the sample. 62

Figure 3-5 Scatter plot showing the relation between N_{eff} and R_s. A negative correlation between N_{eff} and R_s was observed in the grains, while the boundaries showed a positive correlation. 69

Figure 3-6 Changes in the current and charge trap density of a MoS_2

monolayer due to light illumination. (a) Current map measured under dark conditions. (b) Map of current change (ΔI) under illumination. (c) Map of the charge trap density under the dark condition (N_{eff_dark}). (d) Map showing changes in charge trap density (ΔN_{eff}) due to illumination. (e) Scatter plot exhibiting a correlation between N_{eff_dark} and ΔI. The slope of the orange fitted line is ~0.9, indicating linear proportionality. (f) Scatter plot of N_{eff} versus R_s under dark and illuminated conditions.Scatter plot showing the relation between N_{eff} and R_s. A negative correlation between N_{eff} and R_s was observed in the grains, while the boundaries showed a positive correlation. 72

Chapter 1

Introduction

1.1 Charge Trap

In solid-state physics, many physical properties of solids are explained by their energy band structures [1-5]. The band theory assumes that a material is completely homogeneous, and it suggests the existence of energy ranges where no states exist. However, in crystalline lattices, there could be various defects such as vacancies, dislocations and grain boundaries [6]. These defects can generate additional electronic states called charge traps, which are localized within band gap regions [7,8]. Charge traps typically restrict the flow of charge carriers by randomly trapping carriers and releasing the carriers after a period of time. On the other hand, charge traps can also assist carrier transport in many cases such as hopping conduction and Poole-Frenkel conduction [5]. Therefore, investigating trap activities are very important to understanding electrical properties of materials. The trap activity, the trap-and-release of charge carriers, induces a fluctuation in the number of carriers in a conduction channel [9-12]. As a result, an electrical signal from an electronic device includes components which randomly fluctuate over time.

1.2 Electrical Noise

Electrical noise is the random fluctuation of electrical signals from electronic devices. Since noise is a crucial factor determining the device performance and provide information about physical mechanisms, understanding noise is essential both for basic researches and device applications. Here, we will briefly discuss about four fundamental types of noise: thermal noise, shot noise, generation-recombination noise, and 1/*f* noise.

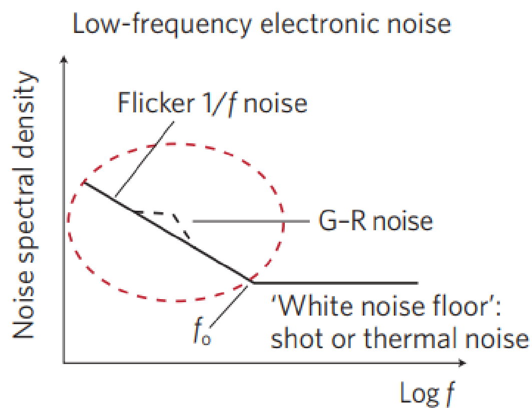

Figure 1-1 Noise spectrum showing fundamental noise [11].

Thermal noise (Johnson-Nyquist noise) is generated by the thermal motion of charge carriers at equilibrium [11-13]. The power spectral density (PSD) of thermal noise is given by

$$S_I = 4kT/R \tag{1}$$

where S_I is the current noise PSD, k is the Boltzmann constant, T is temperature, and R is resistance. Since the thermal noise is frequency independent until quantum oscillation (hf) becomes comparable with kT, it is the white noise.

Shot noise comes from the discreteness of electric charges and unavoidable random fluctuations of electric current. The PSD of shot noise is proportional to current and given by [11-13]

$$S_I = 2qI \tag{2}$$

where q is an electric charge and I is average current. Like thermal noise, shot noise is also frequency independent and becomes white noise.

Generation-recombination (G-R) noise is caused by carrier number fluctuations due to the random transition of charge carriers between bandgap states, that is, charge traps. The G-R noise exhibits a Lorentzian PSD which is expressed as [11,12]

$$S_I = \overline{(\Delta N)^2} \frac{I^2}{N^2} \frac{4\tau}{1 + (2\pi f \tau)^2} \tag{3}$$

where N is the number of carriers, $\overline{\Delta N^2}$ is the variance of N, and τ is relaxation time associated with a specific charge trap. At low frequencies ($2\pi f\tau \ll 1$), the PSD becomes f-independent. On the other hand, at high frequencies ($2\pi f\tau \gg 1$), the PSD follows a $1/f^2$ behavior.

$1/f$ noise (flicker noise) is common noise which is observed in a wide variety of electronic channels at low frequency range. As its name implies, the PSD of $1/f$ noise is given by [11-15]

$$S_I = \alpha \frac{I^2}{f^\gamma} \tag{4}$$

where α is a constant parameter and γ is a scaling factor which is close to 1. Among many explanations, the McWhorter model [15] explains $1/f$ noise by carrier number fluctuations induced by a number of charge traps. The McWhorter model suggests that $1/f$ noise is the superposition of *G-R* noise from various traps where charge carriers are randomly trapped and released with different relaxation times. According to the model, if the relaxation time of traps are distributed within τ_1 and τ_2, the PSD can be written as [11-13]

$$S_I = \overline{(\Delta N)^2} \frac{I^2}{N^2} \int_{\tau_1}^{\tau_2} \mathrm{g}(\tau) \frac{4\tau}{1 + (2\pi f \tau)^2} \, d\tau \tag{5}$$

where $\mathrm{g}(\tau) \sim 1/\tau$ is the distribution function of τ when the trap depths are uniformly distributed. The integration gives the $1/f$ spectrum in the frequency range $1/\tau_2 \ll f \ll 1/\tau_1$. The analysis of $1/f$ noise can give plenty of information on charge traps and their activities in a material.

1.3 Scanning Noise Microscopy

Studies on noise have been based on the statistical analysis of noise data obtained from multiple electronic devices [16]. However, such a method is used to measure the total noise generated by all noise sources distributed on a device, and cannot provide information about the nanoscale distribution or individual properties of local noise sources. Further, it is difficult to exclude device-to-device variations. To overcome these limitations, a noise imaging method named as 'scanning noise microscopy' was developed by Seunghun Hong's group [16,17].

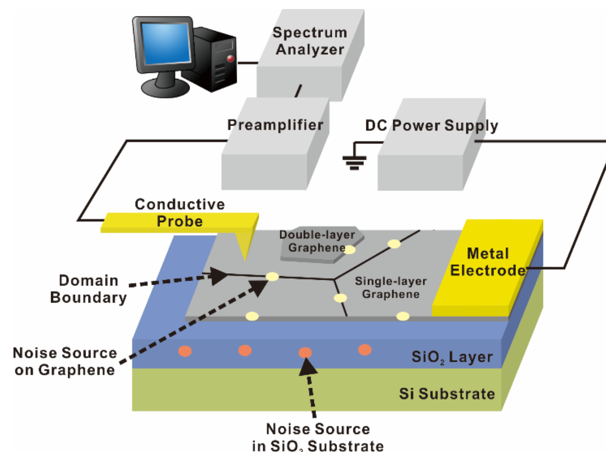

Figure 1-2 Schematic diagram depicting the experimental setup of scanning noise microscopy on graphene [17].

As shown in Figure 1-2, the noise microscopy is the combined system of a conducting atomic force microscopy (AFM), a spectrum

analyzer, and a noise analysis software. In this method, a conducting probe makes a direct contact with the surface of a channel material and measure local electrical current and noise at a specific location. Hence, by laterally scanning the probe over a surface area, one can obtain the current and noise maps of the area. Further, current and noise maps are analyzed to calculate the map of local noise source distribution with nanoscale resolution. Noise microscopy is a simple but versatile tool for investigating noise and other physical properties of various electronic materials.

1.4 References

[1] Ashcroft, N. W.; Mermin, N. D. *Solid State Physics*; Holt, Rinehart & Winston: New York, 1976.

[2] Zaanen, J.; Sawatzky, G. A.; Allen, J. W. *Phys. Rev. Lett.* **1985**, *55*, 418.

[3] Han, M. Y.; Özyilmaz, B.; Zhang, Y.; Kim, P. *Phys. Rev. Lett.* **2007**, *98*, 206805.

[4] Anisimov, V. I.; Zaanen, J.; Andersen, O. K. *Phys. Rev. B.* **1991**, *44*, 943.

[5] Stallinga, P. *Adv. Mater.* **2011**, *23*, 3356-3362.

[6] Henderson, B. *Defects in crystalline solids*; Edward Arnold: London, 1972.

[7] Grasser, T. *Microelectron. Reliab.* **2012**, *52*, 39-70.

[8] Yu, Z.; Pan, Y.; Shen, Y.; Wang, Z.; Ong, Z.-Y.; Xu, T.; Xin, R.; Pan, L.; Wang, B.; Sun, L. et al. *Nat. Commun.* **2014**, *5*, 5290.

[9] Hung, K. K.; Ko, P. K.; Hu, C.; Cheng, Y. C. *IEEE Trans. Electron Devices* **1990**, *37*, 654-665.

[10] Magnone, P.; Crupi, F.; Giusi, G.; Pace, C.; Simoen, E.; Claeys, C.; Pantisano, L.; Maji, D.; Ramgopal Rao, V.; Srinivasan, P. *IEEE Trans. Device Mater. Reliab.* **2009**, *9*, 180−189..

[11] Balandin, A. A. *Nat. Nanotechnol.* **2013**, *8*, 549.

[12] Irwin, J. D.; Wilamowski, B. M. *Fundamentals of Industrial Electronics*; CRC Press, 2016

[13] Song, Y.; Lee, T. *J. Mater. Chem. C*, **2017**, *5*, 7123-7141.

[14] Hooge, F. N.; Kleinpenning, T. G. M.; Vandamme, L. K. J. *Rep. Prog. Phys.* **1981,** *44*, 479-532.

[15] Mcwhorter, A. L. *Phys Rev* **1955,** *98*, 1191-1192.

[16] Sung, M. G.; Lee, H.; Heo, K.; Byun, K.-E.; Kim, T.; Seo, D. H.; Seo, S.; Hong, S. *ACS Nano* **2011,** *5*, 8620-8628.

[17] Lee, H.; Cho, D.; Shekhar, S.; Kim, J.; Park, J.; Hong, B. H.; Hong, S. *ACS Nano* **2016,** *10*, 10135-10142.

Chapter 2

Noise-source Switching in

Phase-separated Organic Nanocomposites

2.1 Introduction

Organic materials have been extensively utilized for various electronic devices due to their superior characteristics such as low power consumption, mechanical flexibility, and suitability for low-cost devices [1-3]. For example, organic field-effect transistors (OFETs) [4], organic light-emitting diodes (OLEDs) [5] and organic solar cells [6] composed of polymers and organic molecules were reported. Furthermore, nanocomposites based on organic materials such as poly(3-hexylthiophene-2,5-diyl) (P3HT), poly(N-vinylcarbazole) (PVK) showed electrical switching behaviors which can be applied to advanced memory devices [7,8]. There have been extensive experimental and theoretical research works for understanding the switching property of organic materials [9-13]. However, an electronic conduction mechanism in nanoscale switching behaviors have not been fully understood yet.

On the other hand, electrical noises in materials are important factors that determine device performances. For instance, it is known that noise sources in a memory device significantly affect switching behaviors, determining operating conditions such as an operation voltage [14,15]. In our previous works, a noise microscopy method based on a conducting atomic force microscopy (AFM) system was developed to investigate the distribution of localized charge traps on a conducting

polymer film [16]. We observed that charge traps play a key role in determining a transport property. However, nanoscale modulations of localized charge traps during a switching process and their effects on the charge transport properties such as conductivity have not been explored before.

In this dissertation, we report the mapping of nanoscale "noise-source switching" phenomena during the optoelectronic switching of phase-separated organic nanocomposites of tetrathiafulvalene (TTF) and phenyl-C_{61}-butyric acid methyl ester (PCBM) molecules dispersed in a polystyrene (PS) matrix. In our method, a nanoscale conducting probe made a direct contact with the nanocomposite film on an ITO electrode, and the maps of electrical currents and noises through the probe were measured. Then, the measured data were analyzed to calculate the maps of conductivity (σ) and charge trap density (N_T) distributions on the nanocomposite film. In the maps, the nanocomposite exhibited phase-separation into *PS-rich* and *TTF-PCBM-rich* phases. At a low applied bias ('off state'), PS-rich phases showed a rather high N_T as compared to TTF-PCBM-rich phases. When a high bias was applied, however, the nanocomposite was 'set' to an 'on state' and the PS-rich phases exhibited a significant decrease in N_T which became lower than that of the TTF-PCBM-rich phases. The results provided evidence for a repeated

modulation in noise sources, which is named here a "noise-source switching", during an electrical switching cycle. Interestingly, we found a scaling behavior of $\sigma \propto N_T^{-1/2}$ which implied the effect of charge traps on electrical conduction. In addition, by exposing UV to the film, we observed optical switching phenomena caused by chemical reactions which gave rise to a decrease in σ and a local increase in N_T. Since our strategy allows us to map a noise modulation during an optoelectronic switching cycle of polymer nanocomposites with a nanoscale resolution, it could be helpful in understanding charge trap behaviors and improving the performance of organic memory devices.

2.2 Experimental Setup

We prepared an organic nanocomposite film composed of TTF, PCBM and PS on an indium tin oxide (ITO) substrate. The polystyrene beads (Product No. 182427, Mw ~ 280,000), PCBM (Product No. 684449), TTF (Product No. 183180) and the common solvent toluene (Product No. 244511) were purchased from Sigma-Aldrich. The low sheet resistance (~8 Ω sq^{-1}) ITO glass (Product No. 703192) was also obtained from Sigma-Aldrich. The 2 mg of each of the TTF, PCBM and PS were separately dissolved in 2 ml of toluene. They were dissolved by applying

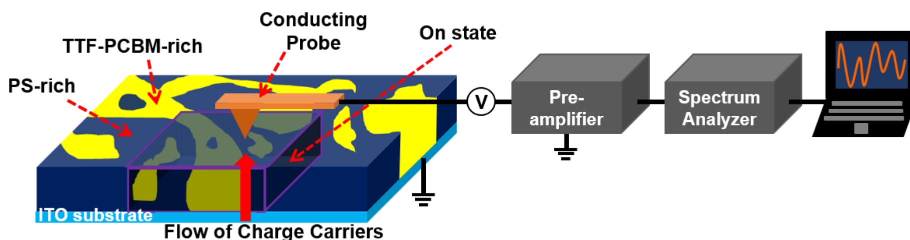

Figure 2-1 Schematic diagram showing our noise microscopy setup for the polymer nanocomposite film on an ITO substrate. The current and noise signals were measured through a biased conducting probe by a homemade spectrum analyzer.

sonication at 60 °C for 90 minutes. The prepared solutions were then mixed together and sonicated for another one hour to obtain the nanocomposite in a solution form. The nanocomposite solution was spin coated on the ITO substrate at 4000 rpm for 60 seconds. The nanocomposite film was heated at 80 °C for 15 minutes.

Figure 2-1 shows the schematic diagram of our current and noise measurement setup. The details of nanocomposite sample fabrication are described in the Experimental Section. For the measurements, a Pt-coated Si tip (Pt300B, Park Systems) installed on an AFM (XE-70, Park Systems) made a direct contact with a nanocomposite film on an ITO substrate. Then, a DC bias was applied to the ITO substrate by a function generator (DS345, Stanford Research Systems). The electrical current through the probe was measured and amplified by a low-noise

preamplifier (SR570, Stanford Research Systems). Electrical noise signals were obtained by filtering the amplified current signals using a band-pass filter included in the preamplifier. The RMS power of noise signals was obtained using a RMS-to-DC converter. By dividing the measured noise power with the bandwidth of the band-pass filter, we can get the noise PSD value at the central frequency of the pass band. Using this system, we could obtain the topography, the current and the noise PSD maps of our sample simultaneously. The measured data were analyzed using a vertical transport model to obtain the conductivity and charge trap density maps of the polymer nanocomposite film.

2.3 Electrical Switching of Organic Nanocomposites

Figure 2-2a shows the chemical structures of TTF, PCBM and PS. Polystyrene has been extensively used as an insulating matrix for nanocomposites due to its chemical inertness and transparency. In a PS matrix, various electronic materials can be dispersed by solution processing, which makes PS useful for a wide range of applications [9,11]. Many organic donor-acceptor complexes dispersed in a PS matrix have shown a switching behavior and electrical bistability [9-11]. For example, *TTF* and *PCBM* in a PS matrix work as *donor* and *acceptor*

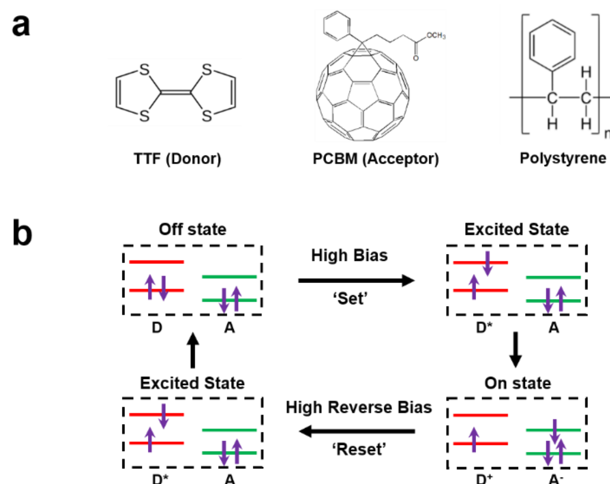

Figure 2-2 (a) Chemical structures of TTF (donor), PCBM (acceptor) and polystyrene (matrix). (b) Charge transfer mechanism in a donor-acceptor complex.

molecules, respectively. The PS-matrix plays a role as a binder and a spacer between TTF-PCBM pairs [17]. The complexes of TTF and PCBM exhibit an excellent switching behavior due to efficient charge generation [11].

It was reported that donor-acceptor pairs can be stabilized by transferring a charge from a donor to an acceptor, forming a charge-transfer complex [18,19]. The formation of a stable TTF-PCBM complex by the charge transfer between TTF (donor) and PCBM (acceptor) molecules has been observed before [11]. Figure 2-2b depicts a reported charge transfer mechanism between donor and acceptor molecules [18].

At a low bias, electrons of donor (D) and acceptor (A) molecules are in ground states ('off state', upper-left). When a high bias is applied, an electron in the highest occupied molecular orbital (HOMO) of a donor can be excited (spin singlet or triplet [20]) to the lowest unoccupied molecular orbital (LUMO) by external electric fields ('set', upper-right). Then, the transfer of the excited electron from a donor to an acceptor occurs since the LUMO energy level of acceptors is lower than that of donors ('on state', lower-right). The 'on state' can be maintained even at a low bias because a strong dipole moment formed in a donor-acceptor pair makes the state very stable, which was reported in organic memory devices based on charge-transfer complexes [12]. Hence, a high reverse bias is needed to return the transferred charge to the donor and 'reset' the state (lower-left). The molecular state goes back to the 'off state' as the excited electron returns to the ground state.

Previously, various conductance switching behaviors have been studied in different polymer nanocomposites. For example, nanocomposite films with only donors or acceptors embedded in insulating matrix (*i.e.* PCBM:PS, PCBM:PI, P3HT:PMMA *etc.*) were reported to exhibit a switching behavior, which was explained by a unipolar switching process based on the modulation of trap activities [21-24]. However, in this case, a rather high bias voltage is required for the

switching process, causing some damages on the insulation matrix [25]. Thus, memory devices based on such films can be unstable and exhibited rather large power consumption [25]. On the other hand, the switching behaviors using the films with different TTF-PCBM concentrations also have been studied before [11,26]. The results showed that such films with different concentrations exhibited just different conductance values without qualitative differences in the switching behavior itself [11,26]. Thus, we chose a TTF-PCBM concentration which has been utilized for stable memory devices and prepared the nanocomposite films with the concentration for our experiments [11].

2.4 Noise-source Switching of an Organic Nanocomposite Film during an Electrical Switching Cycle

Figure 2-3a shows an AFM topography image on a polymer nanocomposite film which consisted of TTF, PCBM and PS. The contact force of a conducting AFM probe to the film surface was maintained as 10 nN during the AFM scanning. The image shows that the nanocomposite film consisted of small grains. The sizes of individual grains were ~500 nm laterally in their diameters. The result shows that a polymer nanocomposite film is comprised of inhomogeneous

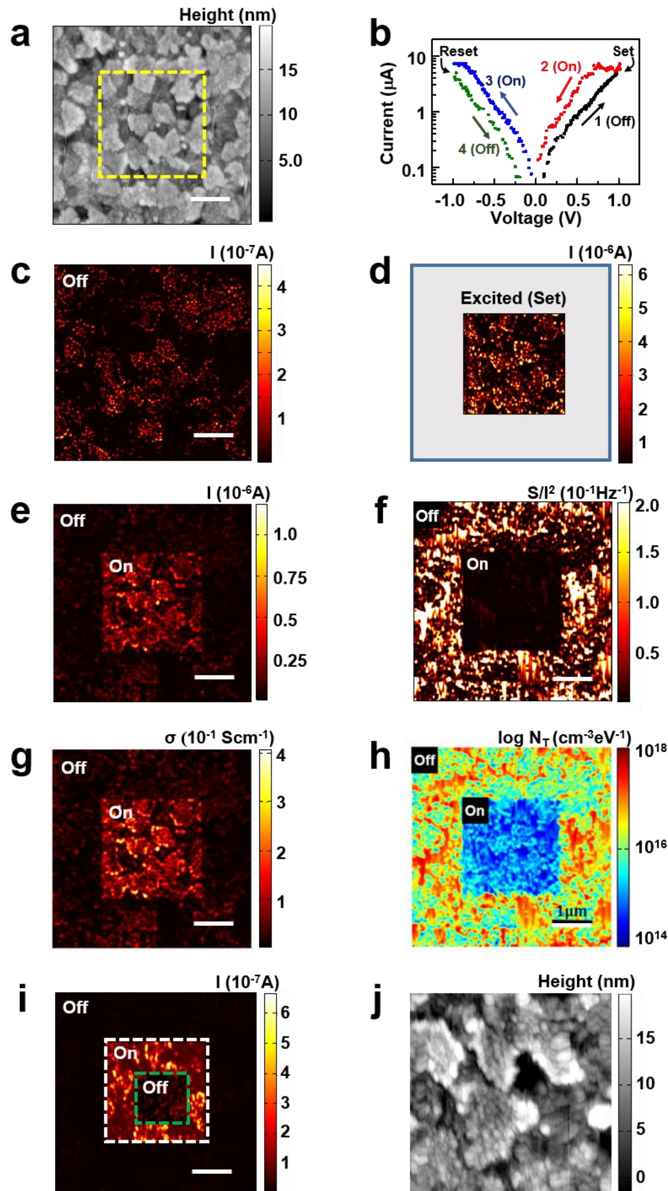

Figure 2-3 Mapping conductivity and charge trap density in the electrical switching cycle of a nanocomposite film. (a) AFM topography image of the nanocomposite film. (b) Current-voltage (*I-V*) curves measured on the sample. (c) Current map measured at the low bias of 0.1 V. (d) Current map measured in an area encircled with a yellow dashed line in (a) at the high bias of 1 V. (e)

Current map obtained at the bias voltage of 0.1 V after the measurement of (d), on the region scanned for (c). (f) Current-normalized noise PSD (S/I^2) map (at 548 Hz) of the nanocomposite. (g) Conductivity (σ) map calculated from the current map in (e). (h) Charge trap density (N_T) map showing the distribution of charge traps on the nanocomposite film. (i) Current map measured at the bias voltage of 0.1 V after we scanned a small region in the 'on state' area with the bias voltage of −1 V. (j) Topography image on the 'reset' region encircled with a green dashed line in (i). Scale bars are 1 μm.

nanostructures, and, the nanoscale study of the film should be essential for the further understanding and improvement of polymer nanocomposite-based devices.

Figure 2-3b shows the current (I) *versus* bias voltage (V) plots on the polymer nanocomposite film of TTF, PCBM, and PS. Here, we prepared the nanocomposite film on an ITO substrate and deposited an Al electrode on the film via a thermal evaporation method. Then, I-V data were measured between the macroscopic Al top electrode and the underlying ITO substrate. When we firstly swept the bias voltage from 0 to 1 V (positive voltages at the Al electrode), the currents were increased with the voltage (black line). Here, a large increase in the currents was observed near the 1 V, indicating the '*set*' of the film. When we measured currents after the set, the currents were about 2-3 times higher than those before the 'set' (red line). To '*reset*' the nanocomposite film, we applied

negative voltages up to −1 V (blue line). After the reset, the sample exhibited the current values similar to those before the set (green line). The hysteresis in the *I*–*V* characteristics shows that the state of our polymer nanocomposite could be reversibly switched between the 'on state' with a high conductivity and the 'off state' with a low conductivity via external bias voltages as reported previously [10-12,19].

Figure 2-3c shows a current map on the polymer nanocomposite film. Here, a DC bias voltage of 0.1 V was applied to the conducting probe, while the ITO substrate was electrically grounded. Then, the current through the probe was recorded while the probe scanned over the film surface to obtain the current map. The current image shows a large spatial variation in current levels even inside individual grains observed in the topography image. Particularly, we could observe that nanoparticle-shaped regions exhibiting high currents of ~10^{-7} A were spread on the polymer film. The particle-like regions had the diameters of about 50 nm. On the other hand, the rest of the region exhibited relatively low current values in the range of 10^{-9} to 10^{-8} A. The result shows that TTF, PCBM, and PS, which are components of the nanocomposite, are non-uniformly distributed over the nanocomposite film. Such phase separation of a polymer composite is commonly observed since it is energetically favorable [27,28]. Though the mixing

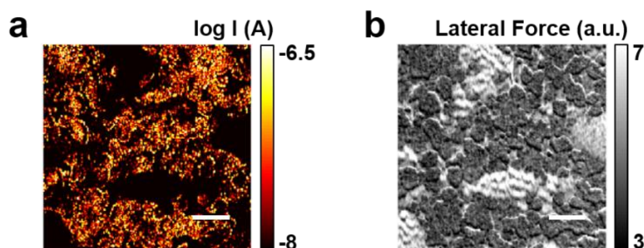

Figure 2-4 Current map and lateral force microscopy image of a polymer nanocomposite film. (a) Current (I) map measured at the bias voltage of 0.1 V. (b) Lateral force microscopy image measured simultaneously with the current map. The image shows a separation between regions of *large* and *small* lateral force, which coincide with *low* and *high* current regions of the current map, respectively.

of constituents is entropically favorable, the entropic driving force is weak since connected monomers in a polymer chain cannot move independently [27]. On the other hand, organic molecules can be mixed well due to the large entropy of mixing. Hence, in our case, TTF and PCBM could be mixed to form a single phase while PS was phase-separated from a TTF-PCBM phase. Considering that PS is an insulator, the *high* and *low* current regions in our polymer composite can be attributed to the *TTF-PCBM-rich* and *PS-rich* phase regions of the nanocomposite, respectively. Previously, it was reported that different phases of a polymer film can be distinguished by a lateral force microscopy due to differences in the surface energy and roughness of the

phases [16]. The lateral force microscopy image of our nanocomposite film (Figure 2-4) showed a clear separation between the regions of *large* and *small* lateral forces matching with those of *small* and *large* currents in the current map, respectively. These results also support the phase separation in our polymer.

Figure 2-3d is a current map on the area encircled with a yellow dashed line in Figure 2a. Here, we mapped current values on the area while applying the high bias voltage of 1 V between the conducting probe and the ITO substrate. Current values were ~4×10^{-6} A in TTF-PCBM-rich phases and ~5×10^{-7} A in PS-rich phases and about an order of magnitude higher than those measured under the low bias voltage of 0.1 V (Figure 2-3c). In this case, a rather high bias voltage of 1V should 'set' the scanned regions of the nanocomposite film to the 'on state'. Also, our nano-resolution current image can show the responses of different-phase-regions in the polymer nanocomposites during the set process with a rather high bias voltage, which should be very useful in nanoscale studies on the polymer nanocomposite.

Figure 2-3e shows a current map, which was obtained after the measurement of the Figure 2d, on the same region as scanned for the Figure 2-3c. Here, the bias voltage of 0.1 V was applied to the conducting probe during the current mapping. In the map, one can clearly identify a

square-shape area much brighter than the other regions. The area exhibits the current level of about 10^{-6} A which is nearly an order of magnitude higher than the other regions. Note that the area corresponds to the region scanned with the conducting probe with the voltage of 1 V to get the Figure 2-3b. The result shows that the electrical conductivity of a specific region on the polymer film can be largely increased by applying a high voltage to the conductive probe and scanning the region with it. This indicates the localized 'set' of the polymer nanocompoiste film, switching the region to the 'on state' from the initial 'off state'. The set process could be successefully done even in nanoscale via local electric fields by a sharp AFM tip, presumably because the conductivity switching of polymer nanocomposites was originated in atomic-scale phenomena such as charge transfer and deep-trap fillings, as previously suggested [10-12,23].

Figure 2-3f shows the map of S/I^2 (at 548 Hz) obtained from the noise PSD map measured simultaneously with the current map in Figure 2-3e. Here, we first measured the map of noise PSD (S) at 548 Hz via the noise microscopy and divided the measured S map by the square of the current map to obtain the S/I^2 map. In the 'off state' region (the outer region), the S/I^2 values were in the range of 10^{-3} to 10^{-1} Hz^{-1}. On the other hand, the 'on state' region (the inner square region) exhibited the

S/I^2 values in the range of 10^{-5} to 10^{-3} Hz^{-1} which are much lower than the S/I^2 in the 'off state' region. This implies that the electrical noise sources can be removed or inactivated by the set process on the polymer composite. In an organic material, various localized electronic states (charge traps) can be induced by defects, impurities and structural inhomogeneity [16,29-33]. And, the random trapping and detrapping of charge carriers by such traps can cause the random fluctuation in the total number of carriers, generating electrical noises [16,29-33]. Previously, it was suggested that the high bias voltage can modify trap occupancy probabilities [23,34]. In our case, such modifications could inactivate charge traps and result in the reduced current noises, as our observation. Considering that electrical noises in organic nanocomposites are a key parameter determining their performance, our result should be very useful in developing the organic nanocomposite-based devices.

Figure 2-3g shows a conductivity (σ) map of the nanocomposite film. We calculated the σ map from the current map at the bias voltage of 0.1 V (Figure 2-3e). In brief, we assumed that charge carriers flew mainly in a vertical direction from the ITO electrode to the conducting probe through the nanocomposite film and parasitic currents in a lateral direction inside the film was limited, because the conductivity of the

nanocomposite was rather low. In this case, a conductivity can be written as $\sigma = Id/(VA)$, where I, d, V and A represent a *measured current*, the *thickness of the film*, an *applied voltage*, and the *contact area of a conducting probe*, respectively. In our experiment, the thickness of the film was ~90 nm. The contact area A of our conducting probe was estimated as ~2000 nm^2 using the same method in our previous study [16]. The σ in the 'off state' region was in the range of 10^{-4} to 10^{-3} S cm^{-1}, whereas the 'on state' region exhibited nearly two orders of magnitude higher σ in the range of 10^{-2} to 10^{-1} S cm^{-1}. These values were consistent with previously-reported electrical conductivities of PS nanocomposites [35]. The σ map quantitatively shows the increase in the electrical conductivity, which was induced by the regional 'set' of the polymer nanocomposite using a conducting probe. Presumably, the increase in the conductivity could be attributed to localized carrier generation in a donor (TTF)-acceptor (PCBM) complex under the conducting probe [10-12] and the filling of deep traps by the generated carriers [34], as previously suggested.

Electrical noises in organic molecules originate in the trapping and detrapping of charge carriers by trap states [16,29-33]. From our current and noise imaging data, we could calculate a charge trap density

(N_T) map (Figure 2-3h) showing the distribution of trap state densities on the polymer nanocomposite film. In this measurement, electrical currents flew vertically between a conducting AFM tip and an underlying ITO film. Thus, the majority of electrical noises should be generated by the charge traps inside the small volume of the polymer nanocomposite film between the ITO electrode and the conducting AFM tip. Then, the PSD of the mean-square fluctuation in the number of occupied charge traps in the small segment of the polymer film within the contact area A of the tip can be written as

$$S_{N_T}(f, x, y) =$$
$$A \int_{-\infty}^{\infty} \int \frac{4\tau(E, x, y, z)}{1 + [2\pi f \cdot \tau(E, x, y, z)]^2} f_t(1 - f_t)\, N_T(E, x, y, z)\, dz\, dE \quad (1)$$

where the N_T, τ, and f are the *density of charge traps over the space and energy*, a *trapping time constant*, and a *frequency*, respectively [16]. The integral over z ranged from 0 to the polymer thickness d. The trap occupancy function can be written as $f_t(E) = [1 + \exp\{(E - E_f) / kT\}]^{-1}$ where E_f is Fermi level. At a rather low temperature condition including a room temperature, $f_t(1-f_t)$ behaves like a delta function around the Fermi level E_f, and the equation (1) after the integral over E can be simplified as

$S_{N_{\mathrm{T}}}(f,x,y) =$

$$A \cdot kT \int \frac{4\tau(E,x,y,z)}{1+[2\pi f \cdot \tau(E,x,y,z)]^2} N_{\mathrm{T}}(E,x,y,z)\, dz \qquad (2)$$

Assuming that charge traps are distributed uniformly over the z direction, the equation (2) can be approximated as

$$S_{N_{\mathrm{T}}}(f,x,y) = A \cdot d \cdot kT \cdot N_{\mathrm{T}}(x,y) \frac{4\tau(x,y)}{1+[2\pi f \cdot \tau(x,y)]^2} \qquad (3)$$

The noise PSD ΔS_{I} can be written as

$$S_{\mathrm{I}}(f,x,y) = \frac{(I)^2}{(\Delta C)^2} S_{N_{\mathrm{T}}}(f,x,y) \qquad (4)$$

where ΔC is the carrier number in the segment of the polymer. Then, the charge trap density N_{T} can be written like,

$$N_{\mathrm{T}}(x,y) = S_{\mathrm{I}}(f,x,y) \frac{(\Delta C)^2}{(I)^2} \cdot \frac{1}{A \cdot d \cdot kT} \cdot \frac{1+[2\pi f \cdot \tau(x,y)]^2}{4\tau(x,y)} \qquad (5)$$

The *average trapping time* τ and the *carrier density* in the polymer were reported as ~10^{-2} seconds and 10^{17} cm^{-3}, respectively [16].

The N_{T} on the 'off state' region was in the range of 10^{16} to 10^{18} cm^{-3} eV^{-1}, whereas the 'on state' region exhibited much lower N_{T} in the range of 10^{14} to 10^{16} cm^{-3} eV^{-1}. The result shows that the nanocomposite

switching by a high bias voltage could also switch the activities of charge traps, as well as the electrical conductivity. Previously, it was reported that a high bias voltage can affect trap activities by filling or releasing charge carriers [23,34]. In our case, it is plausible that a trap filling by carriers generated in the donor-acceptor complex lead to the observed changes of a charge trap density. This is the first observation of a trap-activity switching in a polymer nanocomposite, providing new insights about switching phenomena in organic materials.

After the measurements in Figure 2-3e and f, we scanned a small region in the 'on state' area while applying the bias voltage of −1 V on the conducting probe, which should 'reset' the nanocomposite films in the region. Then, the current map was measured on the nanocomposite film with the bias voltage of 0.1 V (Figure 2-3i). In the map, the region scanned with the bias voltage of −1 V was indicated by encircling it with a green dashed line. The map shows that the 'reset' region has similar current levels with those in the 'off state' region. This indicates that the 'on state' region in the organic nanocomposite could be re-transformed to the 'off state' by the reset process with the high negative voltage of −1 V on the conducting probe, indicating the reversibility of the switching process.

Figure 2-3j shows a topography image on the 'reset' region in Figure 2-3i. When compared with those before the set and reset processes, the topography image did not show any significant apparent changes. The height changes in the topography images during the entire switching cycle was less than 2% from its original thickness. This indicates that the switching was not the result of changes in the thickness or roughness of the nanocomposite film. Instead, electrical effects such as charge transfer in a donor-acceptor complex and a trap filling could lead to the reversible switching of the nanocomposite, as suggested previously [9-12,19].

2.5 Effect of Charge Trap Activities on Local Carrier Transport in an Organic Nanocomposite Film

Figure 2-5a, c, e, g show scatter plots about the relationships between the conductivity (σ) and charge trap density (N_T) of the nanocomposites in 'off' and 'on' states and during the 'set' and 'reset' of a switching cycle. Each data point in the plots represents the σ and N_T values of each pixel area in the region encircled with a green dashed line in Figure 2i at each stage of the switching cycle. Figure 2-5b, d, f, h show the energy level diagrams of the nanocomposite sample, depicting charge transport and trap activities at each stage of a switching cycle. The diagrams exhibit the Fermi levels of an ITO electrode (black line), a Pt-based conducting

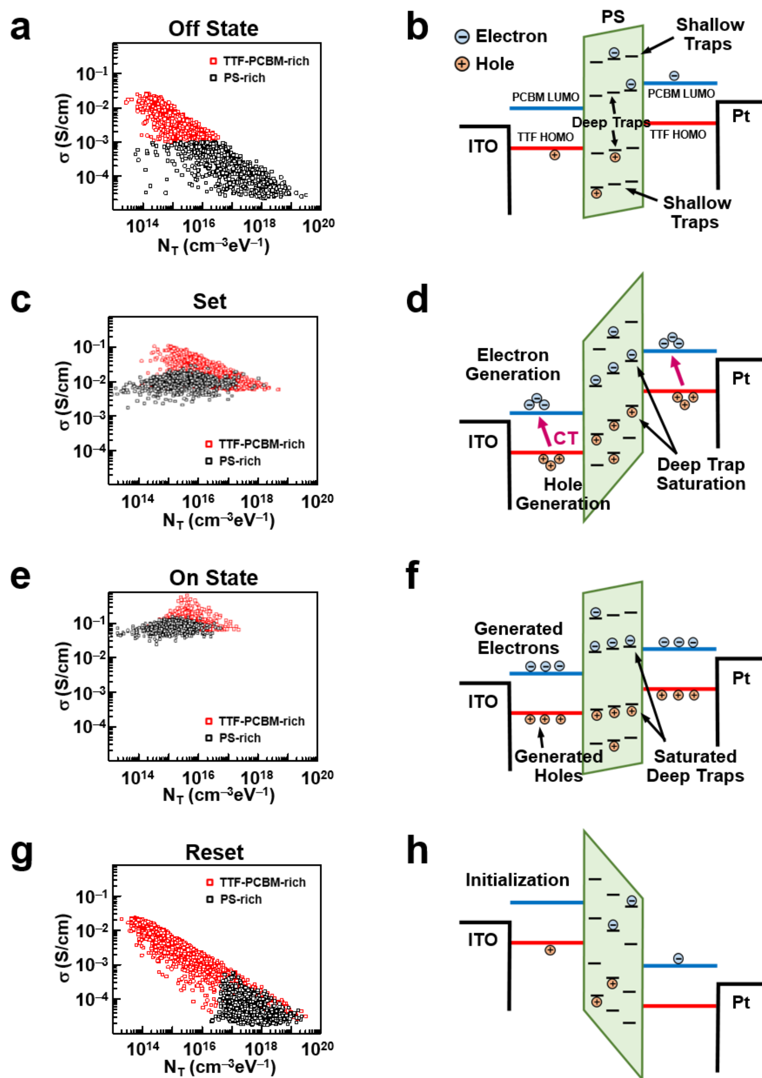

Figure 2-5 Relations between the conductivity (σ) and charge trap density (N_T) of the nanocomposite sample and schematics depicting charge transport and trap activities at each stage of a switching cycle. (a) Scatter plot σ and N_T in an 'off state'. Data from *TTF-PCBM-rich* and *PS-rich* phases are shown with *red* and *black* colors, respectively. (b) Energy level diagram of an 'off state' at the bias of 0.1 V. (c) σ *versus* N_T plot when the sample was 'set' by a high bias. (d) Energy level diagram during a set process with the high bias of 1 V. (e) σ *versus*

N_T plot after the nanocomposite was 'set' to an 'on state'. (f) Energy level diagram of an 'on state' at the bias of 0.1 V. (g) σ *versus* N_T plot when the sample was 'reset' by a high reverse bias. (h) Energy level diagram during a reset process with the negative bias of −1 V.

probe (black line), the lowest unoccupied molecular orbital (LUMO) of PCBM (blue line), the highest occupied molecular orbital (HOMO) of TTF (red line) and the band gap of insulating PS (green box) [36-38]. The HOMO of PCBM and the LUMO of TTF are omitted in the diagrams since they are not relevant to a conduction mechanism. Previous works show that, in PS, many trap states exist within a band gap with a wide distribution in energy [39]. The electron and hole traps near band edges (shallow traps) and near the midgap (deep traps) of PS are marked with short black lines in the diagrams.

Figure 2-5a exhibits the σ *versus* N_T plot of the nanocomposite in an 'off state'. We calculated the σ and N_T from the current and noise maps measured when the bias voltage of 0.1 V was applied to the Pt-based probe. For clarity, the data points of *TTF-PCBM-rich* and *PS-rich* phases are shown with *red* and *black* colors, respectively. The same color convention is adopted to other figures, as well. Based on the observation in the current map of Figure 2-3c, we regarded regions which showed current values *above* and *below* 10^{-7} A in the current map to *TTF-PCBM-*

rich and *PS-rich* phases, respectively. In the plot, the *PS-rich* phases showed much lower σ and higher N_T as compared to the *TTF-PCBM-rich* phases. This could be attributed to that PS is an insulator and has many trap states induced by nanoscale disorders in polymer chains [16,39]. Here, we can observe a negative correlation between the σ and N_T. Specifically, the σ was found to be inversely proportional to the 0.5 power of the N_T ($\sigma \propto N_T^{-1/2}$). This observation directly shows that the N_T is closely related with the σ on our organic nanocomposite film.

Organic nanocomposites are strongly localized systems whose electrical transport is dominated by a hopping conduction [40,41]. Figure 2-5b shows an energy level diagram when the nanocomposite was in an 'off state'. When the bias voltage was applied, electrons in the LUMO of PCBM and holes in the HOMO of TTF were transferred and injected to PS. Since the band gap of PS is large, it became a high potential barrier which obstructed the tunneling of charge carriers from TTF and PCBM. Further, a few carriers injected to PS were trapped by many shallow and deep traps, as described in the diagram. These trap activities could reduce the mobility of carriers. In disordered organic materials like polymers, there are many traps and hopping sites distributed over energy. Since traps are mostly localized in a band gap while hopping sites are localized

near band tails, traps are separated from hopping sites by a trap depth, E_T [40,41]. Here, E_T is defined as a difference between the mean energies of traps and hopping sites, and it can affect the electrical property of a material. For example, the carrier mobility (μ) was reported to be inversely proportional to the trap or charge trap density as $\mu \propto N_T^{-k}$, where the exponent k depends on E_T [40,41]. The k is close to 1 when E_T is very large compared to the energy distribution widths of traps and hopping sites. On the other hand, when E_T is not large and is comparable to the distribution widths of traps and hopping sites, the k is less than 1 [40]. Hence, from a relation $\sigma = ne\mu$, we can consider the $\sigma \propto N_T^{-1/2}$ relation of our sample as the case of $k \sim 1/2$. Some variations of the k from 1/2 could come from a difference on carrier concentrations (n) between the local regions of the nanocomposite film.

Figure 2-5c shows the σ *versus* N_T plot of the nanocomposite film when it was 'set' by the high bias voltage of 1 V on the conducting probe. The plot exhibits a large increase in the conductivity of both TTF-PCBM-rich and PS-rich phases. In the TTF-PCBM-rich phases, σ increased by an order of magnitude and ranged from 6×10^{-3} to 10^{-1} S cm^{-1}. The σ of the PS-rich phases was in the range of 3×10^{-3} ~ 3×10^{-2} S cm^{-1}, indicating the increase by two orders of magnitude. Meanwhile,

the N_T of the PS-rich phases drastically decreased whereas the N_T of TTF-PCBM-rich phases increased. Note that some regions of PS-rich phases showed rather low N_T values compared with the PS-rich phases. The result indicates that the switching of σ and N_T occurred, and the changes on σ and N_T were not uniform over the nanocomposite, depending on the component of a phase. The increase in σ and N_T of the TTF-PCBM-rich phases suggests that both carriers and defects were generated. Previously, it was reported that a high electric field could generate charge defects such as polarons as well as charge carriers [16]. In the PS-rich phases, the increase in σ and decrease in N_T could be attributed to a high electric field and a deep-trap filling [11,34].

Figure 2-5d depicts the energy levels when the nanocomposite was 'set' by the high bias voltage of 1 V on the Pt probe. Under the high voltage, charge transfer (CT) from the HOMO of TTF to the LUMO of PCBM occurred via the mechanism described in Figure 2-2b [10,11]. Consequently, electrons were generated in the LUMO of PCBM and holes were generated in the HOMO of TTF [11], as illustrated in the diagram. When a large number of generated carriers were injected to PS (strong injection), deep traps in PS could be nearly saturated and inactivated [34]. Hence, the carriers were trapped mainly by the shallow

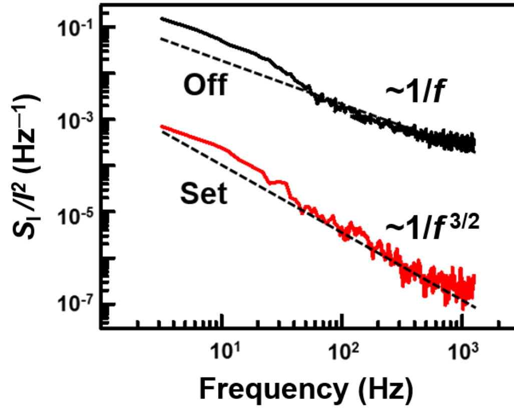

Figure 2-6 Frequency dependence of current-normalized noise PSD (S/I^2) in an 'off state' (black) and during a set process (red). The S/I^2 of an 'off state' exhibited a $1/f$ noise behavior. On the other hand, a $1/f^{3/2}$ behavior was observed in the set process.

traps of PS and they could be easily detrapped due to strong electric fields (Poole-Frenkel emission) [11,34], as illustrated. Therefore, more carriers tunneled the nanocomposite layer at the high bias.

We measured the S/I^2 *versus* frequency (f) spectra of the nanocomposite film at two different stages of a switching cycle (Figure 2-6). Here, currents through the probe were measured and analyzed using a fast Fourier transform (FFT) signal analyzer (SR770, Stanford Research Systems). The 'off state' spectrum was measured at the bias voltage of 0.1 V and the 'set' spectrum was measured when the nanocomposite was 'set' by the bias voltage of 1 V. The '*off state*' and

'*set*' spectra are represented by *black* and *red* curves in Figure 2-6, respectively. Each curve shows a nearly constant slope, indicating $1/f^{\gamma}$ noise behaviors. The exponent γ is estimated as ~*1* and ~*3/2* in the '*off state*' and '*set*' spectra, respectively. In our previous work, we showed that when electrical noises were generated by a large number of trap states with a large variation of trapping times, we observed a $1/f$ noise behavior [16]. The $1/f$ behavior in the 'off state' indicates that the electrical noises were generated by many shallow and deep traps in the nanocomposite film. On the other hand, a $1/f^{3/2}$ noise behavior was suggested to originate in diffusion transport, the number fluctuation of particles in Brownian motion or unstable deep trap states [23,42,43]. In our case, the $1/f^{3/2}$ behavior of the 'set' spectrum could be attributed to unstable trapped charges in the deep traps of PS [23]. When the nanocomposite was 'set' by a high bias voltage, deep traps in PS were nearly saturated and inactivated by generated carriers from charge transfer. Hence, the S/I^2 level of the 'set' curve is lower than that of the 'off state' curve. However, due to a high electric field, some trapped charges in deep traps could not remain stable and they were detrapped from the traps. This trapping-detrapping of the charges in deep traps caused fluctuations in the number of current paths, leading to the $1/f^{3/2}$

behavior [23]. The influence of shallow traps on the noise might be small at the high bias [39].

Figure 2-5e shows the σ *versus* N_T plot of the nanocomposite in an 'on state'. The σ and N_T were calculated from the current and noise maps measured at the bias voltage of 0.1 V after the set process. The plot shows much higher σ and lower N_T than those of the 'off state' shown in Figure 2-5a, indicating that the nanocomposite was 'set' to an 'on state'. The 'on state' exhibited the σ and N_T values which were comparable, but not identical, to those of the set process. There were an increase in σ and a decrease in N_T of both TTF-PCBM-rich and PS-rich phases which could be attributed to the reduced bias voltage of 0.1 V after the set process. Presumably, the decrease in N_T came from the reduction of an electric field, which suggests that trap activities could be affected by the applied bias after the set process. And, the increase in σ can be explained by an increase in carrier mobility due to the decreased N_T [40,41]. Though the inverse proportionality of σ to N_T became rather ambiguous after the set process, data points of high σ values at each N_T value (upper-right boundary) showed the $\sigma \propto N_T^{-1/2}$ behavior.

Figure 2-5f shows an energy level diagram when the nanocomposite was in an 'on state', and the bias voltage of 0.1 V was

applied on the Pt probe. The carriers generated by charge transfer in the set process could be retained even at the low bias due to the formation of a strong dipole moment between donor and acceptor molecules, and the high conductivity state was maintained by an internal electric field induced by the dipole moment [12]. The saturation of deep traps could also be retained since deeply trapped charges in PS take very long time (~10^8 s) to be relaxed due to the low conductivity of PS as previously reported [44]. However, it should be mentioned that the situation can be very different at the high bias conditions (~1V) right after the set process. At the high bias of 1 V ('set'), some charges trapped in deep traps were reported to be unstable [23] and trapping-detrapping of the charges in deep traps led to the $1/f^{3/2}$ noise behavior (Figure 2-6). In this case, some saturated deep traps even with filled charges can still work as noise sources, resulting in a rather large charge trap density N_T. On the other hand, at the reduced bias of 0.1 V, charges trapped in deep traps became stable due to the reduced electric field [23]. Hence, the saturated deep traps could no longer trap charge carriers, which led to the reduced N_T observed in Figure 2-5e.

Figure 2-5g exhibits the σ *versus* N_T plot of the nanocomposite when it was 'reset' by a high negative bias of −1 V. In the plot, the

distributions of σ and N_T values are similar to those of the ‘off state’ in Figure 2-5a, indicating the reversibility of a switching process. The ‘reset’ of σ and N_T could be attributed to the depolarization of a donor (TTF)-acceptor (PCBM) complex and the initialization of molecular states [12]. However, it should be noted that the distribution in PS-rich phases (black circles) is a bit different from that before the switching process (Figure 2-5a). Presumably, the high bias voltage during the switching process caused unavoidable damages on rather insulating PS regions as reported previously [45].

The energy level diagram of the reset process is shown in Figure 2-5h. Under the high reverse bias, a carrier concentration decreased since the charge carriers transferred from TTF to PCBM in the set process returned to TTF. And hence, the deep traps of PS were no more filled with charge carriers, recovering trap activities. These changes could ‘reset’ the nanocomposite to an ‘off state’.

2.6 Optical Switching of Organic Nanocomposite by UV Exposure

Figure 2-7a is a schematic diagram showing a setup for UV exposure on specific regions of our nanocomposite films. We utilized the photomask of array patterns which consist of alternate transparent (10 μm width)

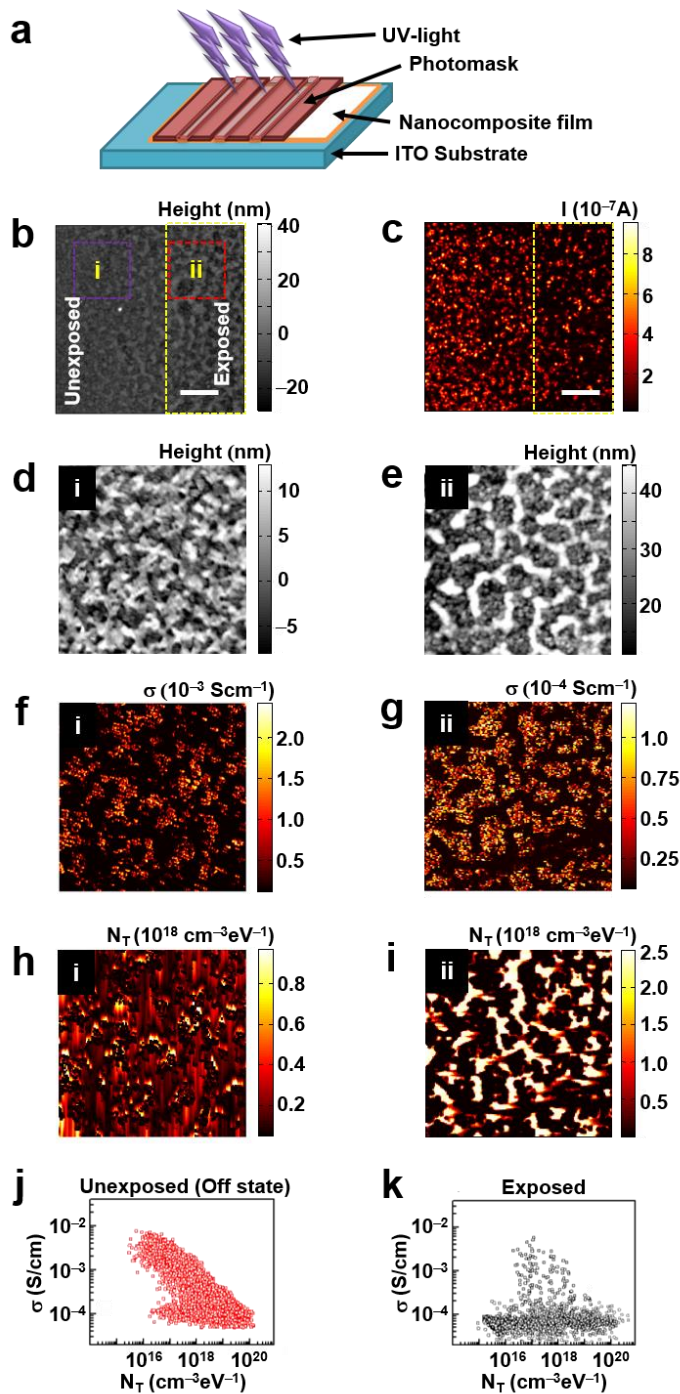

Figure 2-7 Effect of an optical switching by UV exposure on the nanocomposite film. (a) Schematic diagram showing a setup for UV exposure on the

nanocomposite sample. (b) Topography image of the film after the UV exposure. The exposed area is encircled with a yellow dashed line. (c) Current (I) map after the exposure, measured at the bias of 0.1 V. (d,e) High resolution topography image of the (d) unexposed and (e) exposed areas. (f,g) Conductivity (σ) map of the (f) unexposed and (g) exposed areas. (h,i) Charge trap density (N_T) map of the (h) unexposed and (i) exposed areas. (j,k) σ *versus* N_T plots for the (j) unexposed and (k) exposed areas. Scale bars are 5 μm.

and opaque (20 μm width) lines to observe relative changes on the nanocomposite due to UV exposure. The photomask was loaded in a mask aligner for photolithography (MA6, Karl Süss) and brought in a close contact with the nanocomposite film. The wavelength of UV was 405 nm and the irradiation power was 7.9 mW cm^{-2}. After exposed to UV for 2 hours, the sample was characterized by noise microscopy measurements.

Figure 2-7*b* and *c* show the *topography* and *current* maps of the UV-exposed nanocomposite film, respectively. We scanned a region which included both unexposed and exposed areas while applying the bias voltage of 0.1 V on the conducting probe. The exposed area is encircled with a yellow dashed line in the maps. In the topography map, the exposed area shows rather large surface roughness (~40 nm) compared with the unexposed area. The current map exhibits a lower current level in the exposed area than in the unexposed area. The result

indicates that both the nanostructure and conductivity of the exposed area were changed. Previously, it was reported that UV-exposure induces chemical reactions in polymer nanocomposites [46,47]. In our case, such reactions could roughen the surface and reduce the conductivity of the nanocomposite film.

For clarity, we performed the high resolution mapping of unexposed and exposed areas. Figure 2-7*d* and *e* show the topography images of *unexposed* and *exposed* areas marked with '*i*' (encircled with a violet dashed line) and '*ii*' (encircled with a red dashed line) in Figure 2-7b, respectively. The unexposed area showed the surface roughness of ~15 nm which was similar to the value previously observed in the topography image of Figure 2-3a. On the other hand, the exposed area exhibited the large surface roughness of ~40 nm. It appeared that some materials protruded out from the surface of the exposed area, indicating that there was some kind of swelling in the nanocomposite after UV exposure. The nanocomposite of the exposed area could undergo a degradation process and produce protrusions on the surface [46,47].

Figure 2-7*f* and *g* show the σ maps of the *unexposed* and *exposed* areas, which were calculated from current maps measured with the topography images in Figure 2-7*d* and *e* at the bias voltage of 0.1 V, respectively. The σ values of the unexposed area were in the range of

10^{-4} ~ 10^{-3} S cm^{-1}, which is consistent with the observation in the 'off state' map Figure 2-3g. In the exposed area, however, σ decreased and became lower than 10^{-4} S cm^{-1} in most of the area. Especially, the protruded regions in the topography image exhibited rather low σ values compared with other regions. These changes indicate that an optical switching of the nanocomposite occurred by UV, which led to the decrease in a conductivity. In organic materials, chemical reactions can be induced by irradiation. Previously, it was reported that UV exposure leads to oxidation reactions and the formation of phenol-like species in aromatic rings of PS [46]. Further, the presence of a light absorber such as PCBM could enhance photocatalytic activities in the nanocomposites. Thus, the lowered σ of the exposed area can be explained by chemical changes and aging effects which could affect the electrical property of the sample. Our result shows that irradiation as well as a high bias voltage can switch an organic nanocomposite, changing the conductivity of a device.

Figure 2-7*h* and *i* show the N_T maps of the *unexposed* and *exposed* areas, respectively. The N_T maps were calculated from the current and noise maps of each corresponding area. The unexposed area exhibited the N_T ranged from 10^{16} to 10^{18} cm^{-3} eV^{-1}, which was similar

to that observed in the N_T map of an 'off state' in Figure 2-3h. On the other hand, the exposed area exhibited the increased N_T of the protruded regions, leading to an increase in a N_T variation in the scanned area. The result implies that charge traps were additionally generated by UV exposure. In our case, the increased charge traps might come from the oxidation of the nanocomposite since oxidation centers in polymers could work as deep traps [48]. The result suggests that UV exposure can be utilized to control the charge traps of a device based on organic nanocomposites.

Figure 2-7*j* and *k* show the σ *versus* N_T plots of the *unexposed* and *exposed* areas, respectively. Each data point represents the calculated σ and N_T values of each area. The plot of the unexposed area shows the scaling behavior of $\sigma \propto N_T^{-1/2}$, as we observed in an 'off state' in Figure 2-5a. However, the exposed area exhibited a drastic decrease in σ in most part of the scanned area, showing no special correlation between σ and N_T. This indicates that the exposed area was 'set' to a low conductivity state by the UV exposure. Since the switching of the nanocomposite was caused by chemical reactions, it would be not easy to 'reset' an exposed area to an initial state. Hence, the result indicates that UV exposure

processes can be used for the permanent writing of organic memory devices.

2.7 Summary

In summary, we could successfully image a nanoscale "noise-source switching" during the electrical and optical switching of a phase-separated organic nanocomposite film. We found *high* and *low* conductivity regions in the nanocomposite, which could be identified as *TTF-PCBM-rich* and *PS-rich* phases, respectively. The PS-rich phases showed a rather high charge trap density N_T compared with the TTF-PCBM-rich phases at an 'off state' with a low applied bias. Interestingly, when the sample was 'set' by a high bias, there was a drastic decrease in the N_T of the PS-rich phases, which can be explained by the saturation of deep traps by carriers generated from charge transfer. With a high reverse bias, the nanocomposite was 'reset' to an 'off state', exhibiting a high reversibility. The results clearly showed that a switching on noise sources occurred in each stage of an electrical switching cycle. We observed a scaling behavior of $\sigma \propto N_T^{-1/2}$ which implied that charge traps can significantly affect electrical transports. Further, under UV irradiation, the sample showed a large decrease in σ and an increase in a

N_T variation by photo-induced chemical reactions, indicating that charge traps in organic nanocomposites can be optically switched by irradiation. Our result shows an important aspect about reversible noise generation and modulation during the switching cycle of polymer nanocomposites, and hence it may have a significant contribution for the basic study of electrical noises and the development of organic memory devices.

2.8 References

[1] Klauk. H; Zschieschang, U.; Pflaum, J.; Halik, M. *Nature* **2007**, *445*, 745.

[2] Sekitani, T.; Zschieschang, U.; Klauk, H.; Someya, T. *Nat. Mater.* **2010**, *9*, 1015.

[3] Forrest, S. R. *Nature* **2004**, *428*, 911.

[4] Horowitz, G. *Adv. Mater.* **1998**, *10*, 365-377.

[5] Burroughes, J. H.; Bradley, D. D. C.; Brown, A. R.; Marks, R. N.; Mackay, K.; Friend, R. H.; Burns, P. L.; Holmes, A. B. *Nature* **1990**, *347*, 539.

[6] Wöhrle, D.; Meissner, D. *Adv. Mater.* **1991**, *3*, 129-138.

[7] Prakash, A.; Ouyang, J.; Lin, J.-L.; Yang, Y. *J. Appl. Phys.* **2006**, *100*, 054309.

[8] Lai, Y. S.; Tu, C. H.; Kwong, D. L.; Chen, J. S. *Appl. Phys. Lett.* **2005**, *87*, 122101.

[9] Scott, J. C.; Bozano, L. D.; *Adv. Mater.* **2007**, *19*, 1452-1463.

[10] Yang, Y.; Ouyang, J.; Ma, L.; Tseng, R. J.-H.; Chu, C.-W. *Adv. Funct. Mater.* **2006**, *16*, 1001-1014.

[11] Chu, C.-W.; Ouyang, J.; Tseng, J.-H.; Yang, Y. *Adv. Mater.* **2005**, *17*, 1440-1443.

[12] Ling, Q.-D.; Liaw, D.-J.; Teo, E. Y.-H.; Zhu, C.; Chan, D. S.-H.; Kang, E.-T.; Neoh, K.-G. *Polymer* **2007**, *48*, 5182-5201.

[13] Bandyopadhyay, A.; Pal, A. J. *Appl. Phys. Lett.* **2003**, *82*, 1215-1217.

[14] Choi, S.; Yang, Y.; Lu, W. *Nanoscale* **2014**, *6*, 400-404.

[15] Yu, S.; Jeyasingh, R.; Wu, Y.; Wong, H.-S. P. *Phys. Rev. B* **2012**, *85*, 045324.

[16] Shekhar, S.; Cho, D.; Lee, H.; Cho, D.-g.; Hong, S. *Nanoscale* **2016**, *8*, 835-842.

[17] Allard, E.; Cousseau, J.; Orduna, J.; Garin, J.; Luo, H.; Araki, Y.; Ito, O. *Phys. Chem. Chem. Phys.* **2002**, *4*, 5944-5951.

[18] Mikhnenko, O.V.; Blom, P. W. M.; Nguyen, T.-C. *Energy Environ. Sci.* **2015**, *8*, 1867-1888.

[19] Sim, R.; Ming, W.; Setiawan, Y.; Lee, P. S. *J. Phys. Chem. C* **2013**, *117*, 677-682.

[20] Etzold, F.; Howard, I. A.; Forler, N.; Melnyk, A.; Andrienko, D.; Hansen, M. R.; Laquai, F. *Energy Environ. Sci.* **2015**, *8*, 1511-1522.

[21] Baral, J. K.; Majumdar, H. S.; Laiho, A.; Jiang, H.; Kauppinen, E. I.; Ras, R. H. S.; Ruokolainen, J.; Ikkala, O.; Österbacka, R. *Nanotechnology* **2007**, *19*, 035203.

[22] Song, Y.; Jeong, H.; Chung, S.; Ahn, G. H.; Kim, T.-Y.; Jang, J.; Yoo, D.; Jeong, H.; Javey, A.; Lee, T. *Sci. Rep.* **2016**, *6*, 33967.

[23] Song, Y.; Jeong, H.; Jang, J.; Kim, T.-Y.; Yoo, D.; Kim, Y.; Jeong, H.; Lee, T. *ACS Nano* **2015**, *9*, 7697-7703.

[24] Park, K. K.; Jung, J. H.; Kim, T. W. *Appl. Phys. Lett.* **2011**, *98*, 193301.

[25] Lanza, M. *Materials* **2014**, *7*, 2155-2182.

[26] Yang, Y.; Ouyang, J.; Chu, C.-W. *U.S. Patent Application No. 11/666,303*, **2008**.

[27] McNeill, C. *Energy Environ. Sci.* **2012**, *5*, 5653-5667.

[28] Morgado, J.; Moons, E.; Friend, R. H.; Cacialli, F. *Adv. Mater.* **2001**, *13*, 810-814.

[29] Rivnay, J.; Jimison, L. H.; Northrup, J. E.; Toney, M. F.; Noriega, R.; Lu, S.; Marks, T. J.; Facchetti, A.; Salleo, A. *Nat. Mater.* **2009**, *8*, 952.

[30] Nicolai, H. T.; Kuik, M.; Wetzelaer, G. A. H.; de Boer, B.; Campbell, C.; Risko, C.; Bredas, J. L.; Blom, P. W. M. *Nat. Mater*. **2012**, ***11***, 882.

[31] Kuik, M.; Wetzelaer, G.-J. A. H.; Ladde, J. G.; Nicolai, H. T.; Wildeman, J.; Sweelssen, J.; Blom, P. W. M. *Adv. Funct. Mater*. **2011**, *21*, 4502-4509.

[32] Jurchescu, O. D.; Hamadani, B. H.; Xiong, H. D.; Park, S. K.; Subramanian, S.; Zimmerman, N. M.; Anthony, J. E.; Jackson, T. N.; Gundlach, D. J. *Appl. Phys. Lett*. **2008**, *92*, 132103.

[33] Kang, H.; Jagannathan, L.; Subramanian, V. *Appl. Phys. Lett.* **2011**, *99*, 062106.

[34] Chiu, F.-C. *Adv. Mater. Sci. Eng.* **2014**.

[35] Qi, X.-Y.; Yan, D.; Jiang, Z.; Cao, Y.-K.; Yu, Z.-Z.; Yavari, F.; Koratkar, N. *ACS Appl. Mater. Interfaces* **2011**, *3*, 3130-3133.

[36] Schlaf, R.; Murata, H.; Kafafi, Z. H. *J. Electron. Spectrosc. Relat. Phenom.* **2001**, *120*, 149-154.

[37] Halasy, S.; Durakiewicz, T. *J. Phys. Condens. Matter* **1998**, *10*, 10815.

[38] Liu, Y.-X.; Summers, M. A.; Scully, S. R.; McGehee, M. D. *J. Appl. Phys.* **2006**, *99*, 093521.

[39] Watson, P. K.; Schmidlin, F. W.; Ladonna, R. V. *IEEE Trans. Dielectr. Electr. Insul.* **1992**, *27*, 680-686.

[40] Fishchuk, I. I.; Kadashchuk, A. K.; Bässler, H.; Weiss, D. S. *Phys. Rev. B* **2002**, *66*, 205208.

[41] Borsenberger, P. M.; Gruenbaum, W. T.; Magin, E. H.; Schildkraut, D. E.; Visser, S. A. *Jpn. J. Appl. Phys*. **1999**, *38*, 117.

[42] Rocha, P. R. F.; Gomes, H. L.; Vandamme, L. K. J.; Chen, Q.; Kiazadeh, A.; de Leeuw, D. M.; Meskers, S. C. J. *IEEE Trans. Electron Devices* **2012**, *59*, 2483-2487.

[43] Nevins, B. D.; Weissman, M. B. *Phys. Rev. B* **1990**, *41,* 1301.

[44] Baeg, K.-J.; Noh, Y.-Y.; Ghim, J.; Lim, B.; Kim, D.-Y. *Adv. Funct. Mater.* **2008**, *18*, 3678-3685.

[45] Zakrevskii, V. A.; Sudar, N. T.; Zaopo, A.; Dubitsky, Y. A. *J. Appl. Phys.* **2003**, *93*, 2135-2139.

[46] Zhang, D.; Dougal, S. M.; Yeganeh, M. S. *Langmuir* **2000**, *16*, 4528-4532.

[47] Belay, A. B.; Zhou, W.; Krueger, R.; Davis, K. O.; Alver, U.; Sorloaica-Hickman, N. *IEEE J. Photovolt*. **2012**, *2*, 148-153.

[48] Graupner, W.; Leditzky, G.; Leising, G.; Scherf, U. *Phys. Rev. B* **1996**, *54,* 7610.

[49] Jayaraman, R.; Sodini, C. G. *IEEE Trans. Electron Devices* **1989**, *36*, 1773-1782.

[50] Celik-Butler, Z.; Hsiang, T. Y. *IEEE Trans. Electron Devices* **1988**, *35*, 1651-1655.

[51] Carbone, A.; Pennetta, C.; Reggiani, L. *Appl. Phys. Lett.* **2009**, *95*, 233303.

[52] Yang, C.-K.; Yang, C.-M.; Liao, H.-H.; Horng, S.-F.; Meng, H.-F. *Appl. Phys. Lett.* **2007**, *91*, 093504..

Chapter 3

Enhancement of Photocurrent by Local Charge Traps in the Grain Structures of Monolayer Molybdenum Disulfide

3.1 Introduction

Atomically layered transition metal dichalcogenides (TMDCs) have emerged as promising two-dimensional materials for future applications [1,2]. Since TMDCs have unique properties, including an intrinsic band gap varying with the number of layers, a direct band gap and strong spin-orbit coupling in monolayers [2-4], they have been widely studied [1-7]. As a typical TMDC material, molybdenum disulfide (MoS_2) has a layered structure with a monolayer thickness of ~0.7 nm [1]. The layers of MoS_2 are held together by weak van der Waals interactions [1,4]. Due to the direct band gap of ~1.8 eV in the monolayer [2], MoS_2 has great potential for device applications, especially in optoelectronics such as photodetectors [5], light-emitting diodes [6] and solar cells [7]. However, the nanoscale characteristics of electrical conduction and photoconduction in the grain structure of a MoS_2 layer are not fully understood.

In many applications, electrical noise is an important factor, which significantly affects the performance of devices [8]. In addition, noise data often provide critical information for understanding the internal structures and defects of electronic materials such as MoS_2, and thus, methods for the measurement of the noise source activities in electronic materials would be very useful tools for engineering high

performance devices for optoelectronic [9] and electrochemical applications [10]. Until now, noise studies for specific materials have usually been carried out using noise measurements on devices based on the materials. For example, the characteristics and origins of electrical noise in MoS_2 devices were revealed by measuring the gating effect on electrical noise in MoS_2-based electrical channels [11-14]. Meanwhile, a method using a conducting atomic force microscopy (AFM) enabled the direct imaging of localized charge traps in materials [15-17]. A previous study utilized this noise microscopy method to obtain a map of the charge traps on a graphene sample [15]. However, noise microscopy analysis of two-dimensional charge transport in a photoconductive channel has not been reported before.

In this dissertation, we report the observation of the nanoscale anomalous enhancement of photoconductivity induced by localized charge traps in the grain structures of monolayer MoS_2. In this work, a nanoscale conducting probe was used to make direct contact on a monolayer MoS_2 sample on a SiO_2 substrate, and, then, scanned laterally while mapping the electrical currents and noise through the probe. Then, the measured current and noise maps were analyzed to obtain maps for the sheet resistance and localized charge trap distributions in the MoS_2 grain structures. The maps clearly show multiple MoS_2 grains with rather

low sheet resistances and charge trap densities compared with their boundaries. Interestingly, unlike other common conducting channels, the sheet resistance inside the grains was found to be inversely proportional to the charge trap density, which was attributed to the unique role of sulfur vacancies working as both charge hopping sites and charge traps in MoS_2. Furthermore, under light illumination, regions with larger charge trap densities exhibited larger photocurrents, indicating that photocurrents were enhanced by charge trap sites. This method provides a valuable insight for the nanoscale effects of charge traps on the photoconductive charge transport, and, thus, can be utilized for various electrical noise research and practical device applications based on two-dimensional materials.

3.2 Experimental Setup

We prepared a large-area monolayer MoS_2 film via a dual-heating zone chemical vapor deposition (CVD) system. The molybdenum trioxide (MoO_3) powder and a carefully cleaned SiO_2 substrate were heated inside a furnace up to ~750 °C, with the sulfur (S) powder heated inside an electric heater up to ~200 °C. The pressure inside a quartz tube was maintained at ~10 Torr with Ar carrying gas.

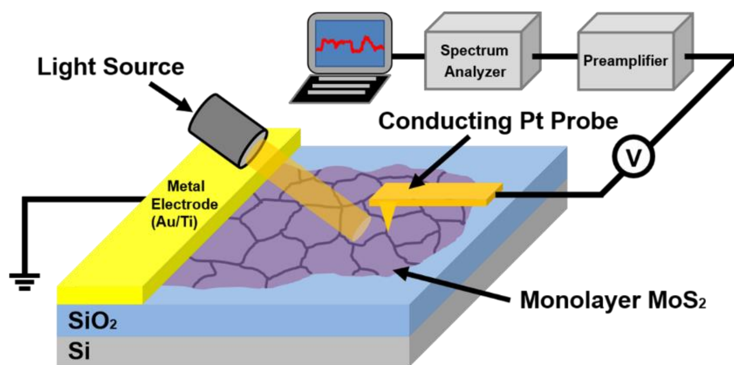

Figure 3-1 Schematic diagram depicting the scanning noise measurement setup for a MoS_2 monolayer sample grown onto a SiO_2/Si substrate. A conducting AFM probe laterally scanned the MoS_2 surface under ambient conditions, while making direct contact with the sample. Electrical current and noise PSD maps were simultaneously measured through the probe. The measured data were analyzed to obtain maps of the sheet resistance and charge trap density distributions in MoS_2 grain structures.

Figure 3-1 shows the schematic diagram of our current and noise measurement setup. A MoS_2 monolayer film was grown onto a SiO_2/Si substrate by a chemical vapor deposition (CVD) method. For the noise microscopy measurement, a Pt-based conducting probe (25Pt300B, Park Systems) installed in an AFM (XE-70, Park Systems) was used to make a direct contact with the surface of the MoS_2 film under ambient conditions. Then, a direct current (DC) bias voltage of 5 V was applied to the Pt probe using a DC power supply (DS345, Stanford Research Systems). The current through the Pt probe was measured and converted

to amplified voltage signals by a low-noise preamplifier (SR570, Stanford Research Systems). Simultaneously, electrical noise (the fluctuating component of a current signal) was collected using a band-pass filter (6 dB) in the SR570 preamplifier. We utilized a homemade root mean square (RMS)-to-DC converter to obtain the RMS power of the noise. The absolute noise power spectral density (PSD) at the central frequency of the band-pass filter was obtained by dividing the square of the measured RMS noise power with the bandwidth of the band-pass filter. Using this setup, two-dimensional maps for the topography, current and noise PSD were obtained at the same time by scanning the AFM probe on the MoS_2 sample. The mapping data were analyzed to obtain maps of the sheet resistance and charge trap density. In addition, we measured changes in the current and noise maps by white light illumination using a light source (LS-F100HS).

3.3 Characterization of a Monolayer MoS_2 Film

Figure 3-2a shows the optical microscopy image of a MoS_2 film. The MoS_2 was synthesized via CVD on a SiO_2/Si substrate. The MoS_2 film exhibited a darker purple color than the SiO_2 region. The constant color contrast of the MoS_2 region implies that the thickness of the MoS_2 film

was rather uniform [18]. The image indicates that the surface of the MoS_2 sample was uniform and clean.

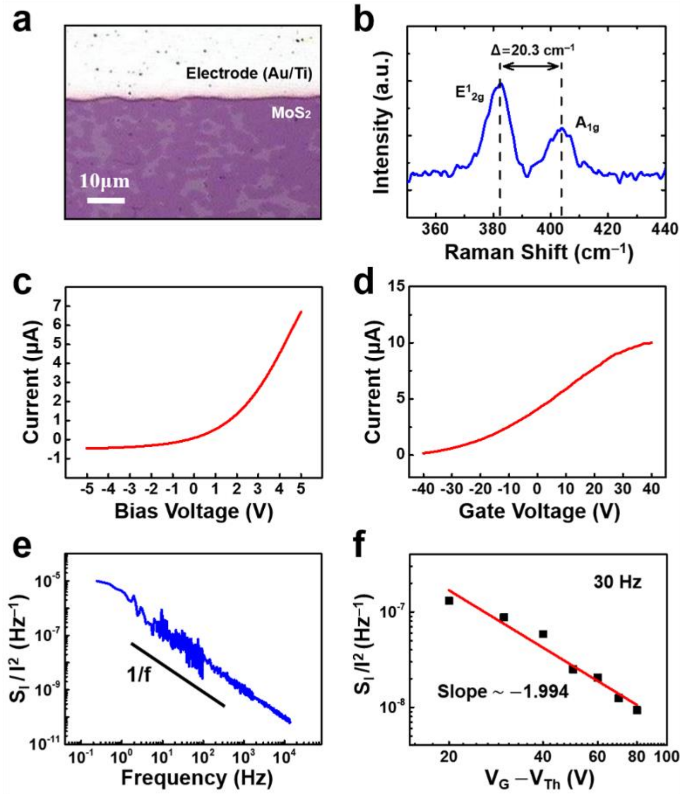

Figure 3-2 Characterization of a monolayer MoS_2 sample. (a) Optical image of monolayer MoS_2 grown onto a SiO_2/Si substrate. (b) Raman spectroscopy data for the sample. (c) Current-voltage (I-V) curve measured on the sample. (d) Current measured by sweeping a gate voltage (V_G). The threshold voltage (V_{Th}) was estimated to be ~−40 V. (e) Current-normalized noise PSD (S_I/I^2) dependence on frequency. (f) S_I/I^2 at 30 Hz as a function of V_G. The slope of the fitted line is −1.994.

The layer number of the MoS_2 film was characterized by Raman spectroscopy (Figure 3-2b). We used a Raman microscope (XperRam 200, Nanobase) with a 532 nm laser. The Raman spectrum of our MoS_2 film shows two major peaks at 383.4 and 403.7 cm^{-1}. The interval for the peaks is approximately 20.3 cm^{-1}. These two peaks correspond to the E^1_{2g} (383.4 cm^{-1}) and A_{1g} (403.7 cm^{-1}) modes of MoS_2 [18]. It is known that the interval for the two major peaks decreases as the number of layers in MoS_2 decreases, being ~20 cm^{-1} in the case of a monolayer [19]. Hence, the Raman spectrum indicates that the MoS_2 film consisted of a single atomic layer. The topography image of the MoS_2 film obtained by AFM measurement also supported the observation of monolayer formation in our film (Figure 3-3).

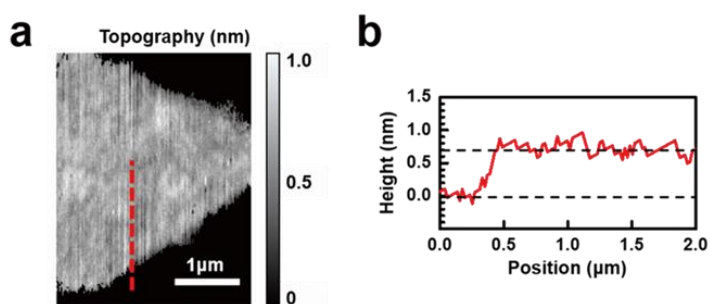

Figure 3-3 Thickness profile of CVD-grown monolayer MoS_2. (a) AFM Topography image of a monolayer MoS_2 sample. Dark regions are SiO_2. (b) Height profile along a red dotted line in (a). The thickness was ~0.7 nm.

Figure 3-2c shows the current-voltage (*I*-*V*) characteristics of our MoS_2 sample. A bias voltage was applied to the Pt probe and swept from −5 to 5 V. The *I*-*V* graph exhibits asymmetric and nonlinear behavior. The nonlinear curve implies that Schottky contacts are formed between the MoS_2 layer and the electrode, presumably due to the large band gap of MoS_2 [20]. Since the work function of the Pt probe is larger than that of the Au/Ti electrode, a negative bias on the Pt probe would worsen the Schottky barrier between the MoS_2 film and the Au/Ti electrode, resulting in a low current level. This result shows the Schottky barrier at the MoS_2-metal contacts may have a significant effect on the *I*-*V* characteristics, as reported previously [21]. Figure 3-2d shows a back gate effect on the sample at a source-drain bias voltage of 3 V. The gate voltage (V_G) was swept from −40 to 40 V using the SiO_2 substrate as a back gate. The result shows an increasing current as the gate voltage was swept from negative to positive values, indicating typical *n*-type behavior for the MoS_2 channel [1,11-14]. The threshold voltage (V_{Th}) (the minimum gate voltage required to form a conducting channel) was obtained from the curve. The threshold voltage (V_{Th}) was estimated to be ~ −40 V, which is the V_G-axis intercept of the extrapolated line for the maximum slope region in the curve. The electrical properties of the MoS_2

sample were comparable to those found in a previous study [18], confirming the uniform quality of our MoS_2 film.

In Figure 3-2e, the frequency dependence of the current-normalized noise PSD (S_I/I^2) is plotted on a log scale. A spectrum analyzer (SR780, Stanford Research Systems) was utilized to measure the noise spectrum. The S_I/I^2 exhibited a $1/f$ noise behavior, as reported in previous noise studies on MoS_2 devices [11-14]. In our previous work, we showed that noise PSDs exhibited $1/f^2$ (or Lorentzian) noise behavior when a current noise was generated by a few trap states that had rather uniform trapping times [15,17]. However, noise spectra exhibited $1/f$ behavior [15-17] when there were many trap states with various trapping times. The $1/f$ noise behavior in our plot implies that the noise was generated by many different noise sources such as charge traps in the MoS_2 sample.

Previously, a $1/f$ noise was suggested to originate from *mobility fluctuations* or *carrier number fluctuations* and that in each case S_I/I^2 is differently related to carrier density [10,11,22,23]. To clarify a dominant origin, we measured S_I/I^2 at different gate voltages (V_G) since the carrier density can be modulated by V_G. Figure 3-2f shows a plot of S_I/I^2 values over V_G. The S_I/I^2 was measured while a V_G ranging from -20 to 40 V was applied to the SiO_2 back gate. The slope of the fitted line in the log-

log plot is estimated to be −1.994, which is close to −2, as expected for *carrier number fluctuations* [14,22,23]. This implies that *carrier number fluctuations* were the dominant mechanism for noise generation in our MoS_2 sample, as reported previously [12,14].

3.4 Mapping of Charge Trap Distribution in the Grain Structure of Monolayer MoS_2

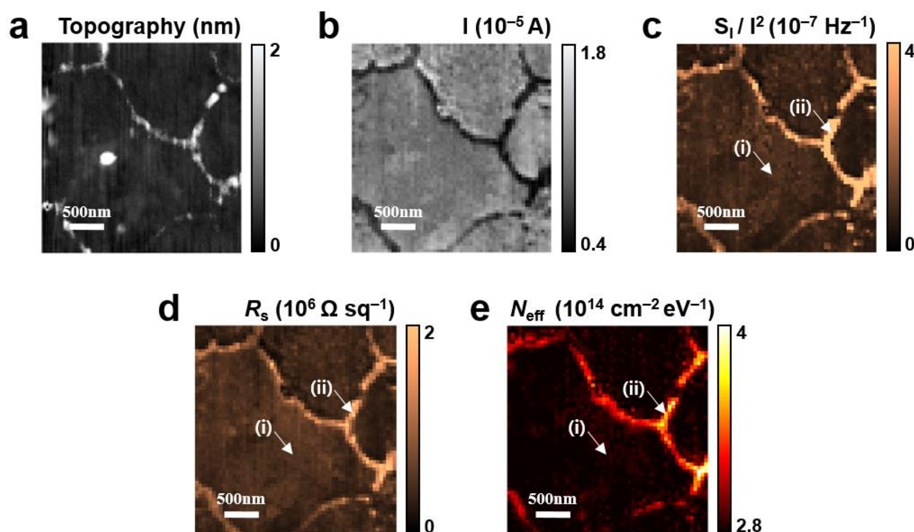

Figure 3-4 Mapping of sheet resistance and charge trap density in the grain structure of a MoS_2 monolayer. (a) AFM topography image of the MoS_2 monolayer film. (b) Current (I) map of the MoS_2 film. A bias voltage of 5 V was applied to the film through a metal electrode. (c) Current-normalized noise PSD (S_I/I^2) map (at 17.3 Hz) for the film. (d) Sheet resistance (R_s) map for the MoS_2 sample. (e) Charge trap density (N_{eff}) map for the sample.

Figure 3-4a shows the AFM topography image of a MoS_2 monolayer. The surface area (3×3 μm^2) was scanned by an AFM probe. In the image, dark regions (film thickness < 1 nm) are distinguished from bright regions (film thickness ~2 nm). Additionally, there is a bright dot near the center of the grain. From the reported thickness of a MoS_2 monolayer (~0.7 nm) [1], we can consider the dark area as grains of MoS_2 and the bright area as grain boundaries. The dot near the center of the grain would be a precursor for the CVD process of a MoS_2 film, as reported previously [24]. The difference in thickness between grain and boundary regions can be explained via a boundary formation mechanism. Typically, the growth of individual grains is known to stop when chemical bonds are formed between the grains [25]. However, it is common that the neighboring grains proceed to grow even after they encounter each other, forming additional layers. Thus, layer-overlapping without chemical bonds can occur, resulting in thicker boundaries [25]. The topography image indicates the cleanliness of the film, which showed no wrinkles or severely rough surface regions.

Figure 3-4b shows a current map for the MoS_2 sample. The current was measured through the conducting probe while a DC bias voltage of 5 V was applied to the Au/Ti electrode. During the measurement, the sample was held under dark conditions to exclude

photocurrents. In the map, bright and dark regions are clearly distinguished. The dark regions (~10^{-6} A), which correspond to boundary regions, showed lower currents compared to the grain regions (~10^{-5} A). This current difference could arise from structural disorder in the boundaries, which obstructs current flow. In a grain boundary region, the atomic structure could be different with that inside the grain due to the different orientation of adjacent grains, or grain overlapping and ruptures. Previous works show that various defects in boundaries, such as line dislocations and complex atomic ring structures, induce mid-gap states and decrease the band gap [26-29]. In addition, grain overlapping and ruptures could generate grain edges with unsaturated bonds, which lead to the intrinsic modification of the electronic structure due to the loss of periodicity [28]. The result shows success mapping of localized currents via a stable contact between the probe and the MoS_2 film, which is important for reliable electrical measurements.

Figure 3-4c shows a S_I/I^2 map (at 17.3 Hz) obtained from a noise PSD map measured simultaneously with the current map (Figure 3-4b). Here, the noise PSD map (S_I) at 17.3 Hz was divided by the square of the current (I) map. The S_I/I^2 values were ~1.12×10^{-7} Hz^{-1} inside a grain (arrowed by (i)) and ~3.96×10^{-7} Hz^{-1} inside a boundary (arrowed by (ii)), indicating a higher noise level in the boundary than in the grain.

The high S_I/I^2 in the boundary implies that a large electrical noise was generated in the grain boundaries. Previously, it was reported that defects and disorders in a MoS_2 layer induce localized states within a band gap [30], which can act as traps [31,32] and generate current noise by trapping and detrapping charge carriers. Hence, the large electrical noise from boundaries can be attributed to rather high density of defects in the area. It is remarkable that noise contributions from each localized area for the monolayer MoS_2 could be distinguished in our result, providing important information about how noise levels differ in grain structures.

Figure 3-4d shows a sheet resistance (R_s) map of the monolayer MoS_2 film. To obtain the R_s distribution, we performed computer calculations based on an iterative method developed in our previous work [15]. In brief, we calculated the R_s map, which reproduced the measured current map in Figure 3-4b, via an iterative method. In the map, grains and their boundaries exhibit a clear difference in R_s. The R_s values were ~8.28×10^5 Ω sq^{-1} inside a grain (arrowed by (i)) and ~2.05×10^6 Ω sq^{-1} inside a boundary (arrowed by (ii)), showing ~2.5 times higher values in boundaries than in grains. The result was consistent with the reported R_s values for CVD-grown monolayer MoS_2 (10^5-10^6 Ω sq^{-1}) [6,26,33]. The large R_s of the boundary regions could originate from

numerous scattering centers due to structural disorder [25,34]. Additionally, the R_s difference between grains and boundaries was similar to that measured for intra- and inter-grain channels in field effect transistors (FETs) in a previous study [26]. However, it should be mentioned that previous measurements had difficulty in clearly distinguishing the localized resistance values for the grains and boundaries since the FET channels included both regions.

From the data in Figure 3-2f, we showed that the $1/f$ noise of our MoS_2 channel (Figure 3-2e) was mainly generated by carrier number fluctuations. The number of carriers fluctuates since charge carriers are randomly trapped and detrapped by charge trap states, generating current noise [35]. Using the differential method developed in our previous study [15], an effective charge trap density (N_{eff}) (the integrated value of the charge trap density over the thickness) of a small area $\Delta x \Delta y$ at (x,y) on a sample surface is obtained as

$$N_{\mathrm{eff}}(f,x,y) = \frac{(\Delta C)^2}{(I)^2} \cdot \frac{f}{kT} \cdot \frac{\Delta S_{\mathrm{I}}(f,x,y)}{\Delta x \Delta y} \qquad (1)$$

where ΔC, I, f, k, T and ΔS_I are the *number of charge carriers*, *measured current*, *frequency*, *Boltzmann constant*, *temperature* and *noise PSD generated by the small area*, respectively. In the case of $1/f$ noise, $\Delta S_I(f,x,y)$ is proportional to $1/f$. Then, $f \cdot \Delta S_I$ becomes f-independent,

resulting in a f-independent $N_{eff}(f,x,y)$, i.e., $N_{eff}(x,y)$. To estimate ΔS_I, we considered a MoS_2 layer as a two-dimensional resistance network. This "network model" was shown to be a successful model in our previous study on graphene samples [15]. The ΔC in equation (1) was estimated from the charge carrier concentration. We calculated the charge carrier concentration (n) using $n = C_{OX} (V_G - V_{Th})/e$, where C_{OX} is the gate capacitance of the SiO_2 layer (~1.48×10^{-8} F/cm^2), V_G is the gate voltage (0 V), V_{Th} is the threshold voltage (~ −40 V), and e is the elementary charge (1.60×10^{-19} C). The calculated value for n was ~3.69×10^{12} cm^{-2}. Then, ΔC could be calculated from $\Delta C = n \Delta x \Delta y$, where $\Delta x \Delta y$ is the effective contact area of the conducting Pt probe (~2000 nm^2). Eventually, we could estimate N_{eff} values at each point of the area scanned by a conducting AFM probe. Since N_{eff} is an integrated value over a thickness, it will be a useful value representing the effective density of charge traps in two-dimensional materials.

Figure 3-4e shows the effective charge trap density (N_{eff}) map of the MoS_2 monolayer. The map exhibits the areal density distribution of the charge traps on the sample. The N_{eff} value was ~2.91×10^{14} cm^{-2} eV^{-1} inside a grain (arrowed by (i)), while the boundary region (arrowed by (ii)) exhibited a N_{eff} value of ~3.87×10^{14} cm^{-2} eV^{-1}, which was ~1.3

times higher in value than that of the grain. In a MoS_2 film, charge traps can be induced by defects including atomic vacancies, dangling bonds and impurities [30-32]. Since defects in monolayer MoS_2 generate trap states within a band gap while defect-free monolayer MoS_2 shows no such states [30,36], N_{eff} corresponds to the density of traps generated by defects. The high N_{eff} in the boundary implies the existence of abundant charge traps, which originate from structural disorder of the boundaries [25,34]. Charge traps in a MoS_2 sample can also be located in the underlying substrate. However, it should be noted that the N_{eff} values in our map were 2-3 orders of magnitude higher than the reported oxide trap density associated with SiO_2 substrates [12,37], indicating that the substrate was not the main origin for the generated noise. Instead, the N_{eff} could be attributed to defects generated during the CVD process under high temperature (~750 °C) and low pressure (~10 Torr), as reported previously [38]. Previously, it was reported that the presence of defects such as sulfur vacancies significantly affects the band structure of monolayer MoS_2 by introducing localized mid-gap states near the Fermi level, leading to a transition from a direct to indirect band gap [30]. Our method provides a method to map localized density of charge traps in two-dimensional nanomaterials, which can be useful for studying charge traps in various other nanostructured materials.

3.5 Effect of Charge Traps on the Hopping Transport of Charge Carriers in Monolayer MoS_2

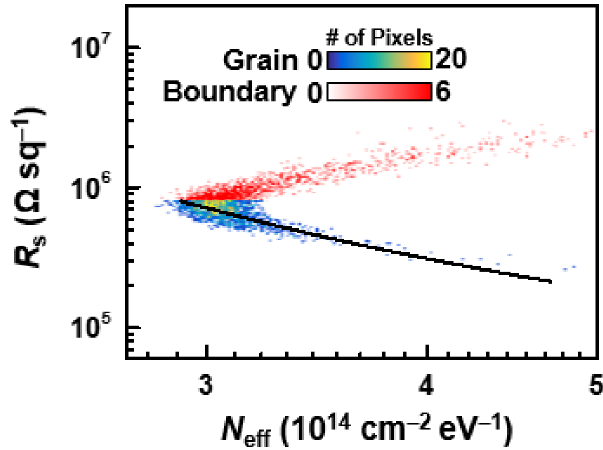

Figure 3-5 Scatter plot showing the relation between N_{eff} and R_s. A negative correlation between N_{eff} and R_s was observed in the grains, while the boundaries showed a positive correlation.

Figure 3-5 shows a scatter plot for the relationship between N_{eff} and R_s for monolayer MoS_2 on a log-log scale. Each data point in the plot is obtained from the pixel area in the N_{eff} map (Figure 3-4e) and the corresponding pixel area in the R_s map (Figure 3-4d). The data points for the grains and boundaries were distinguished using the R_s map. The plot exhibits different tendencies for grain and boundary regions, showing a positive correlation in boundaries and a negative correlation in grains.

The positive N_{eff}-R_{s} correlation in boundaries is similar to previously reported results on the relation between noise PSD and resistance in percolated systems [38-41]. Since boundaries are highly disordered regions with many trap states, each pixel region in the boundaries can be considered as a localized percolation channel. In such a system, it was reported that both resistance and its fluctuation have a power law dependence on $(p-p_{\text{c}})$, where p is the fraction of the conductive paths and p_{c} is the percolation threshold [39]. Hence, the resistance of each pixel region (R_{s}, in our case) is related to its fluctuation as follows

$$\frac{\Delta S_R}{(R_s)^2} \propto (R_s)^w \qquad (\text{at } p > p_{\text{c}}) \tag{2}$$

where ΔS_{R} is the PSD of R_{s}. From $N_{\text{eff}} \sim (\Delta S_{\text{I}} / I^2) = (\Delta S_{\text{R}} / R_{\text{s}}^2)$, the relation $N_{\text{eff}} \sim (R_{\text{s}})^w$ is obtained, which explains the correlation between N_{eff} and R_{s}. In our result, the exponent w was approximately 0.4, which is similar to that observed in an FET channel including the grain boundary in monolayer MoS_2 [40]. This kind of scaling behavior has been observed in many percolation systems where the exponents varied according to the material, geometry and temperature [38-41].

On the other hand, the unique negative correlation for the grain regions can be explained by the electrical transport mechanism in

monolayer MoS_2. It was suggested that the charge transport in few-layered MoS_2 is dominated by hopping through localized states, which originates from sulfur vacancies [14,30,42]. At room temperature (~300 K), the dominating transport mechanism in MoS_2 should be nearest-neighbor hopping [30]. In this mechanism, the conductivity (σ) is expressed as $\sigma \sim \exp(-1/a^2kTN_\mu)$, where '$a$' is an average defect distance and N_μ is the density of states near the Fermi level, which corresponds to N_{eff} [30]. The equation indicates that if there are many sulfur vacancies in a region (high N_{eff}), the hopping probability for the carriers will be high due to the high density of vacancy-induced hopping sites, resulting in a high conductivity. In the plot, the data points for the grain regions are fitted well by the equation $R_s \sim \exp(1/a^2kTN_{eff})$. As a fitting parameter, the average defect distance (a) was estimated to be ~1.97 nm, which was very close to the reported value of ~1.7 nm [30]. Previous observations based on transmission electron microscopy (TEM) revealed that sulfur vacancies are the most common defects in monolayer MoS_2 [30,36]. Additionally, it should be mentioned that the reported density of trap states from sulfur vacancies was comparable to our N_{eff} value [30]. Therefore, the negative correlation between N_{eff} and R_s for the grain regions could be attributed to the sulfur vacancies playing a key

role for both *charge transport* and *charge trap generation* in monolayer MoS_2.

3.6 Photocurrent Enhancement by Local Charge Traps Generated from Sulfur Vacancies of Monolayer MoS_2

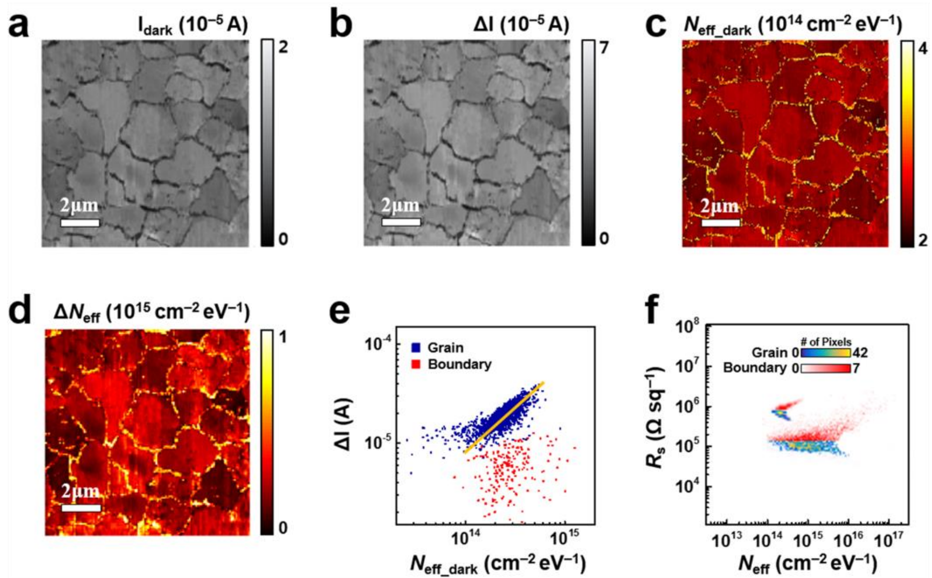

Figure 3-6 Changes in the current and charge trap density of a MoS_2 monolayer due to light illumination. (a) Current map measured under dark conditions. (b) Map of current change (ΔI) under illumination. (c) Map of the charge trap density under the dark condition (N_{eff_dark}). (d) Map showing changes in charge trap density (ΔN_{eff}) due to illumination. (e) Scatter plot exhibiting a correlation between N_{eff_dark} and ΔI. The slope of the orange fitted line is ~0.9, indicating linear proportionality. (f) Scatter plot of N_{eff} *versus* R_s under dark and illuminated conditions.

To investigate the effect of charge traps on photoconductive charge transport in monolayer MoS_2, we measured the MoS_2 film under dark and illuminated conditions. Figure 3-6a shows a current map (I_{dark}) of the MoS_2 monolayer measured under the dark condition. A DC bias voltage of 5 V was applied to the Au/Ti electrode. In the map, many grains were observed since we scanned an area (10×10 μm^2) larger than that of individual grains. The *grains* and *boundaries* were distinguished by relatively *high* and *low* current values, respectively.

Figure 3-6b is the map of the current changes (ΔI) caused by light illumination. We used a white light source (LS-F100HS, Light Bank) with an intensity of ~100 mW/cm^2. Here, a current map was first measured under the dark condition, with the measurement repeated under illumination. After illumination, the currents in the grains were found to increase by more than 10^{-5} A, resulting in ~7.5 times higher current values than before illumination. On the other hand, the currents in the boundaries increased by only a factor of ~4, indicating rather small changes (10^{-6}-10^{-5} A). The current increase was caused by photocarrier generation in the MoS_2 layer [9,43]. Previously, defects such as charge traps in MoS_2 were reported to assist the recombination of photogenerated carriers as recombination centers, and, thus, to reduce the photocurrents [43], which explains the low photocurrent in

boundaries. It is also notable that there were clear differences in current values between individual grains. The current differences between individual grains were as large as 30 % of the average current value of all the grains. This inter-grain current difference can be attributed to an energy band modulation that presumably arises from the random crystal orientation and strain of MoS_2 grains grown via the CVD method [24,34].

Figure 3-6c shows a map of the charge trap density when the MoS_2 film was under the dark condition (N_{eff_dark}). The N_{eff_dark} map was calculated using the current map (Figure 3-6a) and the noise PSD map at 17.3 Hz. The N_{eff_dark} values were on the order ~10^{14} cm^{-2} eV^{-1} and found to be higher in boundaries than in grains. This result is consistent with that shown in Fig. 3-4e. The difference in N_{eff_dark} between individual grains could arise from the grain-growing process, as mentioned in Figure 3-6b.

Figure 3-6d shows a map of the charge trap density changes (ΔN_{eff}) in the MoS_2 film due to illumination. The map was obtained by subtracting the N_{eff_dark} map (Figure 3-6c) from a N_{eff} map measured under light illumination. The ΔN_{eff} map shows a considerable increase in the number of charge traps. The average values for ΔN_{eff} were ~2.85×10^{14} cm^{-2} eV^{-1} in grains and ~7.03×10^{14} cm^{-2} eV^{-1} in boundaries. This

result was in accordance with previous studies showing that light irradiation can increase the charge traps in MoS_2 layers by the removal of atoms due to lattice sublimation [44,45]. On the other hand, O_2 or water molecules physisorbed onto MoS_2 surfaces can work as a charge traps. Such physisorbed molecules could be removed by light illumination, reducing the charge trap density N_{eff}. The large increase in charge trap density in our experiments indicates that charge trap generation by light illumination overwhelmed the effect of the desorption of such physisorbed molecular species.

Figure 3-6e shows a scatter plot showing the relation between the charge trap density under the dark condition N_{eff_dark} and photocurrent level ΔI in the grains and boundaries of the MoS_2 film. Each data point in the plot represents N_{eff_dark} and ΔI values for the pixel area shown in Figure 3-6b and c. In the plot, the data points for the boundary regions show no special correlation. However, a positive correlation between N_{eff_dark} and ΔI is observed in the grain regions, as indicated by the yellow fitted line with a slope of ~0.9. Considering that traps were previously reported to act as recombination centers, resulting in a decreased photocurrent [46], this result is quite unusual. One possible explanation for this anomalous enhancement of the photocurrent by charge traps is

that the photocurrent in few-layer MoS_2 is significantly affected by O_2 molecules on the MoS_2 surface [43,47]. Previous studies showed that both dark current and photocurrent levels for monolayer MoS_2 were much lower in ambient air than in vacuum, attributing the difference to chemisorbed O_2 molecules, which captured a large portion of the electrons from MoS_2 [43,47]. When the MoS_2 was illuminated with light under ambient conditions, electron-hole pairs were generated by photoexcitation. Then, the photogenerated holes recombined with the electrons captured by some chemisorbed O_2 molecules, and the discharged O_2 molecules were desorbed from the surface [43,47]. In this case, the photogenerated electrons, which might be captured by the chemisorbed O_2 molecules, were now free and acted as a charge carrier. Thus, the number of free electrons in the MoS_2 channel increased, and the current increase (ΔI) should be proportional to the number of desorbed O_2 molecules generated by illumination. On the other hand, before illumination, the O_2 molecules were chemisorbed on sulfur vacancies [9] which were responsible for N_{eff_dark}. In this case, the MoS_2 regions with *more sulfur vacancies (or larger* N_{eff_dark}) should have *more chemisorbed* O_2 *molecules* before illumination [30,36], and, following light illumination, they should also have a *larger number of desorbed* O_2 *molecules* and *a larger current increase*. Therefore, the proportional

relationships lead to the proportionality between ΔI and N_{eff_dark}, explaining the fitted line with a slope close to 1 in the log-log plot. Our result revealed the anomalous enhancement of the photocurrent due to charge traps, which can be important in applications of MoS_2 to optoelectronics since electrical noise is often a key parameter determining device performance.

Figure 3-6f shows a scatter plot showing the distributions of the N_{eff} and R_s values for the monolayer MoS_2 under dark and illuminated conditions. Each data point represents the N_{eff} and R_s values of each pixel area in the maps. There are two groups of data points obtained under dark (high R_s) and illuminated (low R_s) conditions. Each group consists of the data points from grains and boundaries, which were distinguished using R_s maps. The distribution of data points obtained under the dark condition was similar to that shown in Figure 3-5, exhibiting different N_{eff}-R_s correlations between grains and boundaries. On the other hand, under illumination, R_s was generally decreased while the distribution of N_{eff} was broadened in both grain and boundary regions. The broadening of the N_{eff} distribution was the result of a large increase in N_{eff} in most regions and a decrease in N_{eff} in only a few regions. The increase in N_{eff} was mainly caused by defect generation due to absorbed photon energy [44,45]. Additionally, localized states filled with charges under the dark

condition could trap charge carriers after photoexcitation of the occupied charges, contributing to the increase in N_{eff}. On the other hand, the desorption of physically adsorbed O_2 molecules from the MoS_2 surface could decrease N_{eff}. It is also worth mentioning that the N_{eff} distribution is rather broadened by the light illumination, resulting in weakened N_{eff}-R_s correlation. Presumably, under dark conditions, most of the charge traps are sulfur vacancies contributing to charge conduction as a hopping site [30]. However, light illumination generated various charge traps, which may not work as a hopping site, such as Mo vacancies and large atomic holes [44].

3.7 Summary

In summary, we successfully imaged how localized charge traps enhanced the photoconductivity in the grain structures of monolayer MoS_2. By laterally scanning a conducting AFM probe used to make direct contact with a monolayer MoS_2 sample, electrical currents and noise transmitted through the probe were simultaneously mapped. The mapping data were analyzed to obtain the distribution maps for the sheet resistance and charge trap density in the grain structures of MoS_2. The result showed that both the sheet resistance and charge trap density were higher in the grain boundaries than in the grains. We found a unique

negative correlation between the charge trap density and sheet resistance, which was attributed to the role of sulfur vacancies acting as both hopping sites and charge traps in monolayer MoS_2. Furthermore, the photocurrent exhibited a positive scaling relation with the charge trap density since photogenerated holes recombined with electrons captured by oxygen molecules absorbed on sulfur vacancies. Since our strategy enabled us to map the nanoscale effect of localized charge traps on the photoconductive carrier transport, it should be a versatile tool that can be used for basic noise studies and applications based on versatile two-dimensional materials.

3.8 References

[1] Radisavljevic, B.; Radenovic, A.; Brivio, J.; Giacometti, V.; Kis, A. *Nat. Nanotechnol.* **2011**, *6*, 147-150.

[2] Mak, K. F.; Lee, C.; Hone, J.; Shan, J.; Heinz, T. F. *Phys. Rev. Lett.* **2010**, *105*, 136805.

[3] Wang, Q. H.; Kalantar-Zadeh, K.; Kis, A.; Coleman, J. N.; Strano, M. S. *Nat. Nanotechnol.* **2012**, *7*, 699-712.

[4] Jariwala, D.; Sangwan, V. K.; Lauhon, L. J.; Marks, T. J.; Hersam, M. C. *ACS Nano* **2014**, *8*, 1102-1120.

[5] Lopez-Sanchez, O.; Lembke, D.; Kayci, M.; Radenovic, A.; Kis, A. *Nat. Nanotechnol.* **2013**, *8*, 497-501.

[6] Yin, Z.; Zhang, X.; Cai, Y.; Chen, J.; Wong, J. I.; Tay, Y.-Y.; Chai, J.; Wu, J.; Zeng, Z.; Zheng, B. et al. *Angew. Chem. Int. Ed.* **2014**, *53*, 12560-12565.

[7] Tsai, M.-L.; Su, S.-H.; Chang, J.-K.; Tsai, D.-S.; Chen, C.-H.; Wu, C.-I.; Li, L.-J.; Chen, L.-J.; He, J.-H. *ACS Nano* **2014**, *8*, 8317-8322.

[8] Hooge, F. N.; Kleinpenning, T. G. M.; Vandamme, L. K. J. *Rep. Prog. Phys.* **1981**, *44*, 479-532.

[9] Nan, H.; Wang, Z.; Wang, W.; Liang, Z.; Lu, Y.; Chen, Q.; He, D.; Tan, P.; Miao, F.; Wang, X. et al. *ACS Nano* **2014**, *8*, 5738-5745.

[10] Xie, J.; Zhang, H.; Li, S.; Wang, R.; Sun, X.; Zhou, M.; Zhou, J.; Lou, X. W.; Xie, Y. *Adv. Mater.* **2013**, *25*, 5807-5813.

[11] Sangwan, V. K.; Arnold, H. N.; Jariwala, D.; Marks, T. J.; Lauhon, L. J.; Hersam, M. C. *Nano Lett.* **2013**, *13*, 4351-4355.

[12] Renteria, J.; Samnakay, R.; Rumyantsev, S. L.; Jiang, C.; Goli, P.; Shur, M. S.; Balandin, A. A. *Appl. Phys. Lett.* **2014**, *104*, 153104.

[13] Sharma, D.; Amani, M.; Motayed, A.; Shah, P. B.; Birdwell, A. G.; Najmaei, S.; Ajayan, P. M.; Lou, J.; Dubey, M.; Li, Q. et al. *Nanotechnology* **2014**, *25*, 155702.

[14] Ghatak, S.; Mukherjee, S.; Jain, M.; Sarma, D. D.; Ghosh, A. *APL Mater.* **2014**, *2*, 092515.

[15] Lee, H.; Cho, D.; Shekhar, S.; Kim, J.; Park, J.; Hong, B. H.; Hong, S. *ACS Nano* **2016**, *10*, 10135-10142.

[16] Shekhar, S.; Cho, D.; Lee, H.; Cho, D.-g.; Hong, S. *Nanoscale* **2016**, *8*, 835-842.

[17] Cho, D.; Lee, H.; Shekhar, S.; Yang, M.; Park, J. Y.; Hong, S. *Sci. Rep*. **2017**, *7*, 43411.

[18] Park, W.; Baik, J.; Kim, T.-Y.; Cho, K.; Hong, W.-K.; Shin, H.-J.; Lee, T. *ACS Nano* **2014**, *8*, 4961-4968.

[19] Lee, C.; Yan, H.; Brus, L. E.; Heinz, T. F.; Hone, J.; Ryu, S. *ACS Nano* **2010**, *4*, 2695-2700.

[20] Yoon, H. S.; Joe, H.-E.; Kim, S. J.; Lee, H. S.; Im, S.; Min, B.-K.; Jun, S. C. *Sci. Rep.* **2015**, *5*, 10440.

[21] Sangwan, V. K.; Lee, H. S.; Bergeron, H.; Balla, I.; Beck, M. E.; Chen, K. S.; Hersam, M. C. *Nature* **2018**, *554*, 500.

[22] Hung, K. K.; Ko, P. K.; Hu, C.; Cheng, Y. C. *IEEE Trans. Electron Devices* **1990**, *37*, 654-665.

[23] Magnone, P.; Crupi, F.; Giusi, G.; Pace, C.; Simoen, E.; Claeys, C.; Pantisano, L.; Maji, D.; Ramgopal Rao, V.; Srinivasan, P. *IEEE Trans. Device Mater. Reliab.* **2009**, *9*, 180−189..

[24] Liu, Z.; Amani, M.; Najmaei, S.; Xu, Q.; Zou, X.; Zhou, W.; Yu, T.; Qiu, C.; Birdwell, A. G.; Crowne, F. J. et al. *Nat. Commun.* **2014**, *5*, 5246.

[25] Najmaei, S.; Liu, Z.; Zhou, W.; Zou, X.; Shi, G.; Lei, S.;

Yakobson, B. I.; Idrobo, J. C.; Ajayan, P. M.; Lou, J. *Nat. Mater.* **2013**, *12*, 754-759.

[26] Ly, T. H.; Perello, D. J.; Zhao, J.; Deng, Q.; Kim, H.; Han, G. H.; Chae, S. H.; Jeong, H. Y.; Lee, Y. H. *Nat. Commun.* **2016**, *7*, 10426.

[27] Huang, Y. L.; Chen, Y.; Zhang, W.; Quek, S. Y.; Chen, C.-H.; Li, L.-J.; Hsu, W.-T.; Chang, W.-H. Zheng. Y. J.; Chen, W. et al. *Nat. Commun.* **2015**, *6*, 6298.

[28] Zhou, W.; Zou, X.; Najmaei, S.; Liu. Z.; Shi. Y.; Kong, J.; Lou, J.; Ajayan, P. M.; Yakobson, B. I.; Idrobo, J.-C.; *Nano Lett.* **2013**, *13*, 2615-2622.

[29] Precner, M.; Polaković, T.; Qiao, Q.; Trainer, D. J.; Putilov, A. V.; Giorgio, C. D.; Cone, I.; Zhu, Y.; Xi, X. X.; Iavarone, M. et al. *Sci. Rep.* **2018**, *8*, 6724.

[30] Qiu, H.; Xu, T.; Wang, Z.; Ren, W.; Nan, H.; Ni, Z.; Chen, Q.; Yuan, S.; Miao, F.; Song, F. et al. *Nat. Commun.* **2013**, *4*, 2642.

[31] Bertolazzi, S.; Bonacchi, S.; Nan, G.; Pershin, A.; Beljonne, D.; Samorì, P. *Adv. Mater.* **2017**, *29*, 1606760.

[32] Yu, Z.; Pan, Y.; Shen, Y.; Wang, Z.; Ong, Z.-Y.; Xu, T.; Xin, R.; Pan, L.; Wang, B.; Sun, L. et al. *Nat. Commun.* **2014**, *5*, 5290.

[33] Schmidt, H.; Wang, S.; Chu, L.; Toh, M.; Kumar, R.; Zhao, W.; Neto, A. H. C.; Martin, J.; Adam, S.; Ozyilmaz, B. et al. *Nano Lett.* **2014**, *14*, 1909-1913.

[34] van der Zande, A. M.; Huang, P. Y.; Chenet, D. A.; Berkelbach, T. C.; You, Y.; Lee, G.-H.; Heinz, T. F.; Reichman, D. R.; Muller, D. A.; Hone, J. C. *Nat. Mater.* **2013**, *12*, 554-561.

[35] Jayaraman, R.; Sodini, C. G. *IEEE Trans. Electron Devices* **1989**, *36*, 1773-1782.

[36] Hong, J.; Hu, Z.; Probert, M.; Li, K.; Lv, D.; Yang, X.; Gu, L.;

Mao, N.; Feng, Q.; Xie, L. et al. *Nat*. *Commun*. **2015**, *6*, 6293.

[37] Na, J.; Joo, M.-K.; Shin, M.; Huh, J.; Kim, J.-S.; Piao, M.; Jin, J.-E.; Jang, H.-K.; Choi, H. J.; Shim, J. H. et al. *Nanoscale* **2014**, *6*, 433-441.

[38] Kim, T.-Y.; Song, Y.; Cho, K.; Amani, M.; Ahn, G. H.; Kim, J.-K.; Pak, J.; Chung, S.; Javey, A.; Lee, T. *Nanotechnology* **2013**, *28*, 145702.

[39] Pennetta, C.; Trefan, G.; Reggiani, L. *Phys. Rev. Lett.* **2000**, *85*, 5238-5241.

[40] Kim, J.-K.; Song, Y.; Kim, T.-Y.; Cho, K.; Pak, J.; Choi, B. Y.; Shin, J.; Chung, S.; Lee, T. *Nanotechnology* **2017**, *28*, 47LT01.

[41] Lee, S. B.; Park, S.; Lee, J. S.; Chae, S. C.; Chang, S. H.; Jung, M. H.; Jo, Y.; Kahng, B.; Kang, B. S.; Lee, M.-J.; Noh, T. W. *Appl. Phys. Lett.* **2009**, *95*, 122112.

[42] Cho, K.; Min, M.; Kim, T.-Y.; Jeong, H.; Pak, J.; Kim, J.-K.; Jang, J.; Yun, S. J.; Lee, Y. H.; Hong, W.-K. et al. *ACS Nano* **2015**, *9*, 8044-8053.

[43] Zhang, W.; Huang, J.-K.; Chen, C.-H.; Chang, Y.-H; Cheng, Y.-J.; Li, L.-J. *Adv*. *Mater*. **2013**, *25*, 3456–3461.

[44] Paradisanos, I.; Kymakis, E.; Fotakis, C.; Kioseoglou, G.; Stratakis, E. *Appl. Phys. Lett.* **2014**, *105*, 041108.

[45] Castellanos-Gomez, A.; Barkelid, M.; Goossens, A. M.; Calado, V. E.; van der Zant, H. S. J.; Steele, G. A. *Nano Lett.* **2012**, *12*, 3187-3192.

[46] Wang, H.; Zhang, C.; Rana, F. *Nano Lett*. **2014**, *15*, 339-345.

[47] Lee, Y.; Yang, J.; Lee, D.; Kim, Y.-H.; Park, J.-H.; Kim, H.; Cho, J. H. *Nanoscale* **2016**, *8*, 9193-9200.

Chapter 4
Conclusions

In this dissertation, the effects of charge trap activities on local carrier transports in inhomogeneous two-dimensional films were investigated by a scanning noise microscopy method.

Firstly, we quantitatively mapped the electrical and optical switching of localized charge traps, the "noise-source switching" phenomena, in an organic nanocomposite of TTF, PCBM and PS. The nanocomposite showed phase-separation into *PS-rich* and *TTF-PCBM-rich* phases. When an applied bias was low, the PS-rich phases exhibited a rather high charge trap density N_T compared with the TTF-PCBM-rich phases at an 'off state'. Remarkably, when the sample was 'set' by a high bias, there was a significant decrease in the N_T of the PS-rich phases, which came from the saturation of deep traps. After a high reverse bias was applied, the nanocomposite was 'reset' and initialized to 'off state'. The result clearly showed repeated switching on noise sources during each stage of an electrical switching cycle. The scaling behavior of $\sigma \propto N_T^{-1/2}$ implied that charge trap activities largely affect electrical conduction. In addition, by exposing UV to the film, we observed optical switching phenomena due to degradation which led to a decrease in σ

and a local increase in N_T.

Secondly, we conducted studies on photocurrent enhancement by localized charge traps in the grain structures of monolayer MoS_2. Here, electrical current and noise from monolayer MoS_2 were measured and analyzed to obtain maps of sheet resistance and localized charge trap distributions. The result showed that both the sheet resistance and charge trap density were lower inside grains than on grain boundaries. Interestingly, we found that sheet resistance was inversely proportional to charge trap density inside the grains, which was attributed to sulfur vacancies acting as both hopping sites and charge traps in monolayer MoS_2. Furthermore, the photocurrent exhibited a positive correlation with the charge trap density since electron-capturing oxygen molecules were chemisorbed on sulfur vacancies.

The results should contribute to the understanding of the nanoscale effects of charge trap activities on electrical conduction and photoconduction in inhomogeneous two-dimensional materials. Further, our method based on a noise microscopy is expected to be a versatile tool for basic noise research and applications.

Chapter 5
Abstract in Korean

초록

불균일한 이차원 필름에서 전하트랩의 활동이 나노 스케일의 국소적인 캐리어 수송에 미치는 영향의 매핑에 관한 연구

결정성 물질 내에는 공공, 전위, 결정립계 등의 다양한 결함이 존재한다. 이런 결함들은 물질의 에너지 밴드 구조의 밴드 갭 영역에 전하 트랩이라 불리는 국소적인 에너지 준위를 생성한다. 이러한 트랩들은 전하 운반자들을 무작위적으로 트랩하고 일정 시간 후에 다시 방출함으로써 전하 운반자들의 흐름을 제한한다. 뿐만 아니라, 트랩들은 전하 운반자의 수송에 크게 관여하기 때문에 트랩의 활동을 조사하는 것은 물질의 전기적 특성을 이해하는데 매우 중요하다. 전하 운반자를 트랩하였다가 방출하는 트랩들의 활동은 전도성 채널 내의 전하 운반자

의 개수에 요동을 일으킨다. 그 결과, 전자 소자에서 측정되는 전기적 신호는 시간에 따라 무작위하게 진동하는 전기적 노이즈 성분을 포함하게 된다. 따라서 전자 재료에서 발생하는 전기적 노이즈를 측정하고 분석함으로써 전하 트랩의 활동에 따른 물질의 고유한 전도 특성과 내부 구조에 관한 귀중한 정보를 얻을 수 있다.

본 연구에서는 전도성 원자힘 현미경에 기반한 주사잡음 현미경법을 사용하여 불균일한 이차원 필름에서 전하 트랩의 활동이 국소적인 전하 운반자의 수송에 미치는 영향에 대하여 논의할 것이다.

먼저, tetrathiafulvalene (TTF), phenyl-C_{61}-butyric acid methyl ester (PCBM) 분자들이 polystyrene (PS)에 분산된, 상 분리된 유기 나노 혼합물에서의 노이즈 발생원의 스위칭 현상에 관해 논의할 것이다. 이 연구에서는 노이즈 현미경을 사용하여 나노 스케일의 해상도로 유기 혼합물 필름의 국소적인 전도도와 전하 트랩 밀도를 매핑하였다. 흥미롭게도, 높은 전압에 의해 유기 나노 혼합물이 'set' 되는 경우에 절연체인 PS 성분이 풍부한 상에서 노이즈 발생원인 활성화된

전하 트랩의 밀도가 크게 감소하는 스위칭 현상이 관찰되었다. 각 물질의 에너지 밴드 구조를 바탕으로, 이 현상은 TTF-PCBM 복합체에서 생성된 전하 운반자들이 PS의 트랩을 채워서 비활성화 시키기 때문임을 밝혔다. 또한 필름의 국소적인 전도도가 전하 트랩의 밀도와 지수 함수 관계를 갖는 것을 확인하였는데, 이는 전하 트랩이 전기적 전도성에 미치는 영향을 정량적으로 밝힌 것이다. 이러한 결과를 통해 유기 메모리 소자의 스위칭 과정에서 전하 트랩의 활동이 미치는 영향과 그 가역적인 변동에 관한 증거를 제시하였다.

다음으로, 이황화몰리브덴 (MoS_2)의 그레인 구조 내에서 국소적인 전하 트랩에 의한 변칙적인 광전도성의 증가에 대해 논의할 것이다. 여기서는 노이즈 현미경을 사용하여 단층 MoS_2를 측정함으로써 처음으로 MoS_2의 그레인 구조에서 나노 스케일의 해상도로 면 저항과 전하 트랩 밀도의 맵을 계산하였다. 맵을 분석한 결과 특이하게도 면 저항과 전하 트랩 밀도 간에 음의 상관관계가 존재함을 발견하였는데, 이는 단층 MoS_2에서 황 원자의 공공이 생성한 에너지 준위가 전하의 호핑 전도에 이용될 뿐만 아니라 전하 트랩의 역할도 하는 고유

한 특성 때문이었다. 또한, 단층 MoS_2에 빛을 쪼인 경우에는 국소적인 전하 트랩에 의해 광전류가 증가하는 현상이 관찰되었다. 이것은 공기 중의 산소 분자가 황 원자의 공공에 화학적으로 흡착된 상태로 있다가 빛에 의해 탈착되면서 전자를 방출하기 때문에 나타나는 현상임을 밝혀내었다.

주요어: 전하 트랩, 결함, 전하 운반자 수송, 전기적 노이즈, 원자힘 현미경, 주사 노이즈 현미경, 이차원 필름

학번: 2012-20370